J. Fluid Mech. (2001), *vol.* 447, *pp.* 299–336.
DOI 10.1017/S0022112001005882 Printed in the United Kingdom

Coalescence, torus formation and breakup of sedimenting drops: experiments and computer simulations

By GUNTHER MACHU[1], WALTER MEILE[1], LUDWIG C. NITSCHE[2] AND UWE SCHAFLINGER[1]†

[1]Institut für Strömungslehre und Wärmeübertragung, Technische Universität Graz, Inffeldgasse 25, A-8010, Graz, Austria

[2]Department of Chemical Engineering, The University of Illinois at Chicago, 810 South Clinton Street, Chicago, IL 60607, USA

(Received 22 February 2000 and in revised form 5 June 2001)

The motion and shape evolution of viscous drops made from a dilute suspension of tiny, spherical glass beads sedimenting in an otherwise quiescent liquid is investigated both experimentally and theoretically for conditions of low Reynolds number. In the (presumed) absence of any significant interfacial tension, the Bond number $\mathscr{B} = (\Delta\rho)gR^2/\sigma$ is effectively infinite. The key stages of deformation of single drops and pairs of interacting drops are identified. Of particular interest are (i) the coalescence of two trailing drops, (ii) the subsequent formation of a torus, and (iii) the breakup of the torus into two or more droplets in a repeating cascade. To overcome limitations of the boundary-integral method in tracking highly deformed interfaces and coalescing and dividing drops, we develop a formal analogy between drops of homogeneous liquid and a dilute, uniformly distributed swarm of sedimenting particles, for which only the $1/r$ far-field hydrodynamic interactions are important. Simple, robust numerical simulations using only swarms of Stokeslets reproduce the main phenomena observed in the classical experiments and in our flow-visualization studies. Detailed particle image velocimetry (PIV) for axisymmetric configurations enable a mechanistic analysis and confirm the theoretical results. We expose the crucial importance of the initial condition – why a single spherical drop does not deform substantially, but a pair of spherical drops, or a bell-shaped drop similar to what is actually formed in the laboratory, does undergo the torus/breakup transformation. The extreme sensitivity of the streamlines to the shape of the ring-like swarm explains why the ring that initially forms in the experiments does not behave like the slender open torus analysed asymptotically by Kojima, Hinch & Acrivos (1984). Essentially all of the phenomena described above can be explained within the realm of Stokes flow, without resort to interfacial tension or inertial effects.

1. Introduction

This paper addresses the behaviour of single drops and pairs of trailing drops made from dilute suspensions of tiny particles, undergoing gravitational sedimentation with negligible effects of inertia and interfacial tension. These conditions correspond to a low Reynolds number and an infinite Bond number, respectively. The phenomena

† Uwe Schaflinger died on 27 April 2000, during the publication process of this paper.

observed for a gravitationally driven motion of drops made of homogeneous liquids or suspensions, a complex shape evolution, including coalescence and breakup, are fundamental to the mechanics of multiphase flows, and have direct and indirect applications in many chemical and pharmaceutical processes. Similar effects occur in geophysical flows: the limit of infinite Bond number applies to rising mantle plumes (Manga, Stone & O'Connell 1993; Manga 1997), and flows involving bubbles in molten rock arise in volcanic processes and *in situ* vitrification (Manga & Stone 1994; Manga 1996; Manga *et al.* 1998). Thus, the specialized but very basic problem of sedimenting drops has motivated a considerable body of experimental and theoretical work, which is described and analysed in § 1.6 following an organized description of the key phenomena observed in our laboratory (§§ 1.2–1.5). Section 2 develops the theoretical basis for simulating drops as a swarm of Stokeslets, and lists algorithmic details of the numerical scheme. The experimental system, procedures, and data reduction are described in § 3. Section 4 combines experiments and theory to distinguish and analyse the flow phenomena described above and provides mechanistic insights.

In order to be precise, we use the term *liquid drop* to describe a connected volume of homogeneous liquid existing within – and distinguishable by some thermophysical properties from – an expanse of another liquid. This identification applies regardless of the chemical composition of the two liquids, their miscibility or immiscibility, and of interfacial tension. For example, even a drop of cold water settling through a vat of hot water (Kojima, Hinch & Acrivos 1984) would qualify under this general definition; the reverse situation is found in rising mantle plumes (Manga *et al.* 1993; Manga 1997). We use the term *suspension drop* to describe a swarm of very small (nearly microscopic) particles that are homogeneously distributed (with respect to macroscopic or statistical properties such as volume fraction, size distribution, etc.) throughout an identifiable, connected volume within an infinite expanse of the suspending liquid. The term 'nearly microscopic' refers mainly to the characteristic spacing between particles and implies that this length scale is so small that the liquid–solid mixture represents an effective continuum of excess mass upon which gravity is pulling, i.e. a pseudo-liquid. The particles are assumed to be sufficiently large that Brownian diffusion is negligible. We shall consider suspensions so dilute that the pseudo-liquid is Newtonian, with a viscosity essentially the same as that of the pure liquid. Under these conditions it is not surprising that a suspension drop behaves essentially like a liquid drop (Kojima *et al.* 1984). The term *blob* applies when the 'physical discretization' represented by the particulate substructure is too coarse to support the continuum view of a pseudo-liquid without some conceptual modification. In the absence of an unambiguous cut-off between suspension drops and blobs, the distinction should be made in operational terms: with increasing size of the particulate substructure, additional physical phenomena come into play beyond the hydrodynamics of a pseudo-liquid. One might say that such substructural effects – notably, hydrodynamic or shear-induced dispersion (Davis 1996; Nitsche & Batchelor 1997) – reside within the 'discretization error' of a blob as compared to a suspension drop. Whether these phenomena can be approximated in continuum terms (e.g. a dispersion or mass transfer coefficient) as opposed to detailed modelling on the particulate scale is a separate question. The important point is that some addition to continuum hydrodynamics must be made in the case of a blob.

For suspension drops and blobs the concepts of shape and (fuzzy) interface are macroscopic interpretations. Usually the meaning is clear visually, but it also eludes a general, unambiguous definition suitable for all cases. For example, if two bulbous lobes are connected by a thin thread, is the assembly now one blob or two? The

answer hinges on the diameter of the thread in relation to both the substructural and bulk length scales.

The analogy between liquid drops and suspension drops has been mentioned only qualitatively in previous papers. One point of our work is to assert that this analogy is, in fact, *fundamental and useful for numerical simulations*. We show in § 2 that, at each instant, the continuum limit of the 'physical discretization' represented by a dilute suspension drop is actually formally equivalent to the quasi-static hydrodynamic equations for a liquid drop with the same viscosity as the surrounding liquid. Thus, computer simulations involving nothing more complicated than a swarm of Stokeslets approximate (in a well-defined sense) the boundary-integral formulation, and capture all of the essential phenomena observed in classical creeping-flow experiments on sedimenting or buoyant drops: coalescence, formation of a ring, and a cascade of ring disintegrations. These interesting effects have not yet yielded to the boundary-integral method because of the difficulty of tracking highly distorted interfaces. The sedimenting Stokeslets function simultaneously as generators of the flow field and as tracers that track the motion and deformation of the drop. Molecular dynamics (MD) has been used to simulate droplet dynamics in particulate terms, both on the nanoscale (Murad & Law 1999; Moseler & Landmann 2000) and approaching larger dimensions (Greenspan 1990). But the underlying premise is totally different, because the molecules or quasimolecular aggregates interact directly through the intermolecular forces. Our particles interact *indirectly* through the point-force continuum flow fields set in motion by gravitational forces. Dissipative particle dynamics (DPD) involves frictional forces acting between particles in response to relative motion, but the typical form (unrelated to the Stokeslet) is truncated beyond a cutoff radius (Jones *et al.* 1999; Clark *et al.* 2000): it represents short-range interactions, not the slow $1/r$ decay characteristic of disturbances in creeping flow. Furthermore, the frictional forces are also accompanied by random forces, as required by the fluctuation-dissipation theorem. It is important to note that any detailed treatment of near-field interactions – for example, the ingenious but highly technical approach developed for Stokesian dynamics simulations (Brady & Bossis 1988) – is not necessary for the class of gravity-driven flows considered here.

Considering both the experimental and computational results to be presented below, the proposition of tracking the distended, convoluted, rolled and folded interfaces with marker points as in the boundary-integral method seems almost hopeless. In contrast, the macroscopic concept of a (fuzzy) interface makes sense independent of the individual identities of the particles that collectively represent the macroscopic shape of a drop at any instant. In fact, the automatic 'renewal' of the interfacial zone with particles from the interior is an incidental part of the volumetric formulation. The resulting robustness of the Stokeslet simulations more than compensates for the additional CPU time and memory needed for the three-dimensional discretization.

In order to avoid cluttering the introduction of basic phenomena with descriptions of previous papers, we first present observations only from our laboratory (§ 1.2–1.5) and then place them in context with respect to the literature of the field (§ 1.6).

1.1. *Dimensionless groups*

The particle Reynolds number $\mathscr{R}_\mathrm{p}$ is based upon the Stokes settling velocity U_p of an isolated spherical particle of radius a and density ρ_p,

$$\mathscr{R}_\mathrm{p} = \frac{U_\mathrm{p} a}{\nu_\mathrm{f}} = \frac{2}{9}\frac{(\rho_\mathrm{p} - \rho_\mathrm{f}) g a^3}{\rho_\mathrm{f} \nu_\mathrm{f}^2}, \tag{1}$$

with g the gravitational acceleration, and ρ_f and ν_f the density and kinematic viscosity, respectively, of the surrounding liquid. For the flow field produced by a small number of sedimenting particles, we may neglect inertia of the liquid if $\mathscr{R}_p$ is small. This criterion applies because (i) there are not enough particles to meaningfully define a macroscopic object with its own length scale, alternative to a, and (ii) the mean velocity among the particles will be of the order of U_p (although somewhat greater, because of mutually induced hydrodynamic disturbances).

When the particles are so numerous that the swarm takes on a meaningful macroscopic identity such as a suspension drop or blob (characterized by the linear dimension R), then the underlying assumptions change. The characteristic velocity U_d of the swarm now reflects a balance of viscous and buoyant forces on the macroscopic length scale R, and greatly exceeds U_p. The drop Reynolds number $\mathscr{R}_d$ is now based upon R and U_d,

$$\mathscr{R}_d = \frac{U_d R}{\nu_f} = \frac{(\Delta\rho) g R^3}{\rho_f \nu_f^2} = \frac{9}{2}\frac{\phi}{\epsilon^3}\mathscr{R}_p, \quad \epsilon = a/R \ll 1, \tag{2}$$

with ϕ the volume fraction of solids and $(\Delta\rho) = \rho_d - \rho_f = \phi(\rho_p - \rho_f)$ the density difference between the liquid–particulate mixture forming the drop and the liquid outside. For dilute suspensions the particles will not significantly alter the viscosity.

In order to neglect inertia of the liquid in the flow field set in motion by a sedimenting suspension drop, we must abandon the particle Reynolds number and impose the much more stringent requirement $\mathscr{R}_d \ll 1$. The blobs in our experiments conformed to the assumption of small drop Reynolds number, and their behaviour was accurately depicted by computer simulations of Stokes flow, for which $\mathscr{R}_d = 0$.

Inertia of the particles in a suspension drop or blob is not important if the viscous–inertial relaxation time is short compared with the time it takes for a particle to move through distance R at the characteristic velocity U_d (Nitsche & Batchelor 1997). Thus we must have a small Stokes number,

$$\mathscr{S} = \frac{m_p/\zeta}{R/U_d} = \left(\frac{2}{9}\frac{\rho_p}{\rho_f}\epsilon^2\right)\mathscr{R}_d \ll 1, \tag{3}$$

with m_p the mass of an individual particle and $\zeta = 6\pi\nu_f\rho_f a$ its Stokes friction coefficient. Inertia of the liquid is clearly the limiting consideration, since $\epsilon \ll 1$.

The degree to which a drop deforms is an outcome of the competition between forces causing deformation and capillary forces tending to restore the drop to a spherical shape. The ratio of the gravitational forces to the latter is the Bond number,

$$\mathscr{B} = \frac{(\Delta\rho) g R^2}{\sigma} \tag{4}$$

with σ the interfacial tension. Currently there is no compelling reason to believe that the (fuzzy) interface between a suspension and clear liquid should support an interfacial tension. Therefore the Bond number is effectively infinite.

1.2. *Single drops*

In figure 1 photographs similar to those presented by Schaflinger & Machu (1999) show the behaviour of a sedimenting swarm of glass particles in glycerin. The first photograph shows the typical shape of the swarm shortly after the downward injection of the suspension below the free surface of the liquid. The lower part of the swarm forms a roughly hemispherical cap, while the upper part resembles the conical shape of the laminar jet formed during the injection process. Clearly visible is that clear

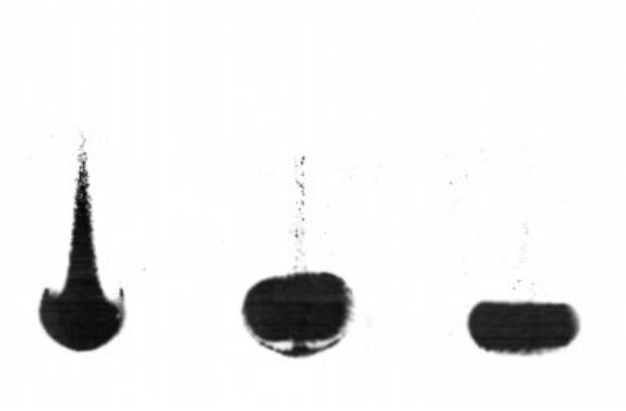

FIGURE 1. Examples of different stages of the shape evolution of a swarm of glass particles sedimenting in pure glycerin, parameter set E2 (table 3).

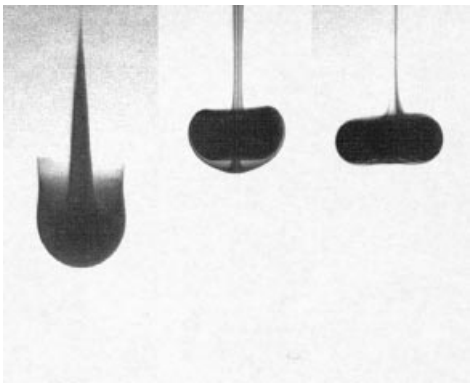

FIGURE 2. Analogous stages of the shape evolution of a liquid drop of glycerin coloured with commercial blue ink, sedimenting in a glycerin-water solution, parameter set E1 (table 3).

liquid starts to become entrained at the upper (rear) part of the suspension drop, and circulates in the toroidal vortex. This causes the mushroom shape with the cap as seen in the second photograph. The suspension drop can also be dropped into the tank from the tip of a needle placed just above the free surface; the shape of the drop once it is completely submerged is approximately the same. This leads to the important observation that – in the absence of interfacial tension – it is nearly impossible to produce in the laboratory the theoretical ideal of a spherical drop (which would then not entrain clear liquid). Such entrainment is the key mechanism for what is illustrated in the third photograph: the evolution of the suspension drop into a ring-like structure, which we refer to generically as a torus. In time, the torus disintegrates, as will be described in § 1.5.

Figure 2 shows similar stages of the evolution of a liquid drop made of pure glycerin and a small amount of commercial blue ink. Although the size, density difference and viscosity ratio do not match those for the suspension drop in figure 1, the three main stages of evolution correspond very closely. The common features for these two cases are (i) a small drop Reynolds number, (ii) negligible interfacial tension and (iii) a viscosity ratio of the order of unity. These pictures alone suggest the fundamental

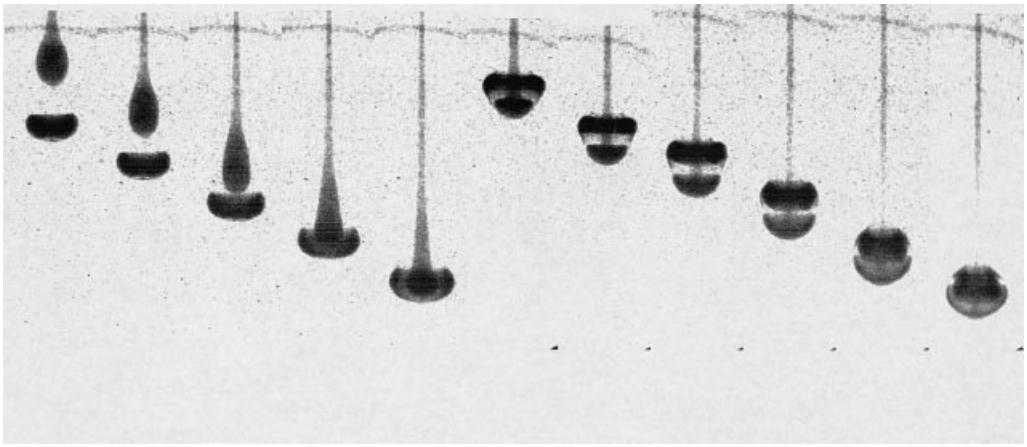

FIGURE 3. The interaction of two trailing suspension drops sedimenting in pure glycerin in an essentially axisymmetric configuration, parameter set E3 (table 3).

nature of the analogy (to be developed in § 2) between suspension drops and liquid drops.

1.3. *Pairs of interacting drops*

Photographs in figure 3 show the interaction and evolution of two vertically displaced, sedimenting suspension drops in an essentially axisymmetric geometry. Basic features of the far-field interaction – namely, converging streamlines upstream of a Stokeslet versus diverging streamlines downstream – have been identified by Manga & Stone (1993) as being responsible for the flattening of the leading (lower) drop into an oblate shape and the elongation of the trailing drop into a prolate shape. There are no capillary effects to oppose these viscous deformations at effectively infinite Bond number. The trailing drop catches up with the leading drop and pokes through, after which both drops begin to mix and the tail becomes disconnected. This mechanism includes entrainment of the surrounding bulk liquid, which subsequently gives rise to the torus as for a single drop.

1.4. *Torus formation and breakup: not all tori are the same*

As has been described in the preceeding subsections, and as will be expanded upon in § 4, the torus represents an intermediate outcome of a range of initial configurations involving one or more drops. Once the torus has formed, however, the subsequent evolution appears always to proceed in two distinct phases. First comes a period of cyclic expansion and contraction (with a prevailing expansion) of the fluid ring, which seems not to have received much specific attention aside from the description in Schaflinger & Machu (1999). Then the ring disintegrates into two or more droplets, each of which forms a torus and disintegrates, and so on in a cascade. A detailed examination of these phenomena will be deferred to § 4. But it is worthwhile here to make one subtle yet crucial point that has been overlooked in all previous investigations: despite the visual similarity, the torus that first forms is different from the torus that eventually disintegrates. This distinction is explicable entirely within the realm of Stokes flow.

As we first observed from the particle image velocimetry (PIV) measurements (figure 4*a*) and then calculated using a swarm of Stokeslets (figure 4*b*), the streamlines do not pass through the centre of the torus that forms initially. For this case we define

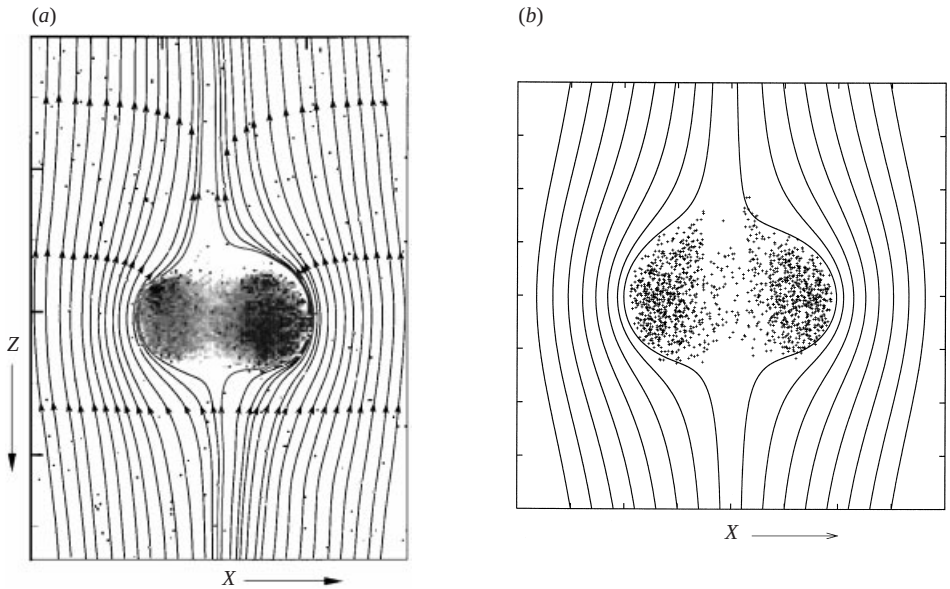

FIGURE 4. Streamline patterns in a sectional plane for two sedimenting rings of suspension: (*a*) PIV measurements for a closed torus, parameter set E4 (table 3), distance between major tickmarks corresponds to 5 mm; (*b*) calculations for a closed torus; parameter set C2.

the term 'stream envelope' as the dividing surface that separates the outer bypassing streamlines from the inner recirculating streamlines. Its presence could be inferred from the pattern of the outer streamlines, which are the only streamlines displayed in figure 4(*a*, *b*). Such an envelope of closed streamlines extends at least partly outside the drop, so that some of the recirculating streamlines run from behind through the interface and 'sweep out' the central portion of particles, which are then carried by the toroidal vortex back to the rear. This is the same mechanism by which liquid initially becomes entrained at the rear of the drop (§ 1.2). We refer to this as a 'closed torus', which has two stagnation points, front and rear. At some point the torus changes to an 'open torus', for which the streamlines then pass through the hole in the centre. This transition is evident from figure 24, which will be discussed in § 4.4. The open torus is not stable and 'bulges develop on the ring . . . ; these fall faster than the rest of the ring . . . and the ring bends and breaks into drops' (Joseph & Renardy 1993, p. 309). The crucial point is this: it is the *closed* torus that first forms and then undergoes cyclic expansion and contraction; it is the *open* torus that eventually disintegrates.

That this surprising mechanistic feature could have escaped detection for so long is understandable because it hinges on an extreme (initially implausible) sensitivity of the streamline pattern to the configuration of the ring; see figures 24 and 5. It must be kept in mind that the flow field is generated solely by gravity 'pulling' on each point (or particle) in the drop, which amounts to nothing more than a volume integral of the Green's function (Stokeslet) for creeping flow. From figure 4(*b*) it appears that the stream envelope forms when even a low density of particles 'plugs' the hole. But figure 5 shows that a stream envelope can also form when the hole is completely unobstructed, if the hole is small enough compared with the overall diameter of the ring (non-slender case). Elongation of the cross-section in the axial direction – for example, a semicircle (*b*) or an ellipse (*c*) – from the circle (*a*) seems to be responsible for the stream envelope and the attendant stagnation points that 'close off' the hole to throughflow.

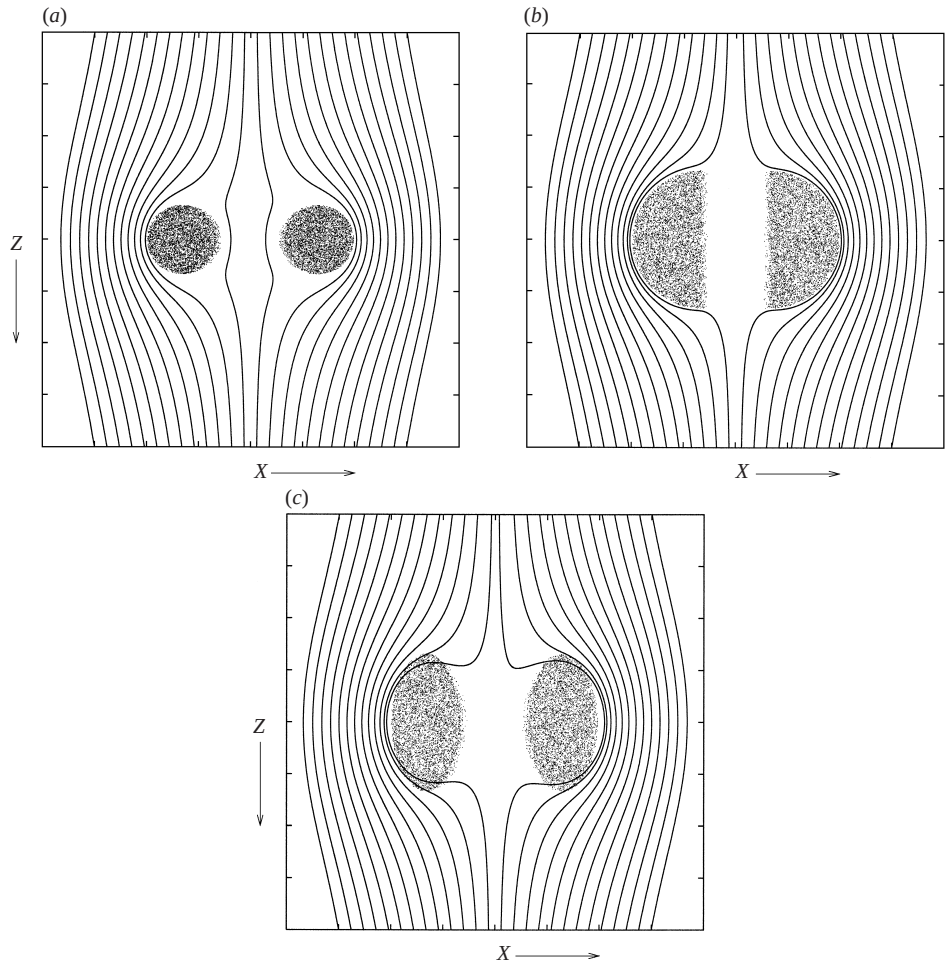

FIGURE 5. Calculated streamline patterns in a meridian plane for three different ring-like swarms containing 60 000 randomly distributed Stokeslets. In each case the outside diameter of the ring is 3 times the diameter of the hole. The cross-sections are (*a*) circular; (*b*) semicircular; (*c*) elliptical with 2 : 1 axis ratio.

For a slender (open) ring, the asymptotic analysis of Kojima *et al.* (1984) showed that inertial effects are necessary to explain expansion of the ring, and that this result holds independently of the cross-sectional shape. This conclusion was, however based on the starting assumption of axisymmetry, by which the three-dimensional instability of a slender open ring (figure 20 below) could not have been detected. We believe that the rings for which they reported experimental data (refer to their table III) were not slender enough for their asymptotics to apply: the smallest radius ratio (cross-section/ring) was 0.35. It is likely that their 'fatter' rings started out as closed tori according to our explanation, which invokes only Stokes hydrodynamics.

1.5. *Behaviour and evolution of the tail*

As mentioned before, the tail emanating from the rear of the suspension drop becomes disconnected under certain circumstances and is left behind. The tail now moves independently of the drop, and somehow represents a 'history' of the drop's

FIGURE 6. Photograph of bulging and breakup of the tail of a suspension drop.

motion and evolution. In time, bulges form with regular spacing along the tail, which spawn smaller droplets – see also Schaflinger & Machu (1999). The new droplets disconnect and behave essentially as described in § 1.2. In figure 6 two photographs of the shape evolution of the tail are shown. In the photograph on the left, the tail begins to bulge, with the subsequent formation shown on the right photograph. Surprisingly, the bulging and droplet formation was not observed for tails created from drops of homogeneous liquid. This phenomenon appears to be the only qualitative difference between the behaviour of suspension drops and liquid drops. At present we can only speculate on the reason for this distinction. Perhaps the bulging of the particle tail is due to the fact that there is an unavoidable distribution of particle sizes in the experiments. This could cause larger particles to overtake smaller particles and form the bulges. Or else the flow might support a basic hydrodynamic instability. Since the particulate scale would assert its substructural presence first in an entity of the smallest bulk dimension (the thin tail), one might also suspect that a sub-continuum effect such as shear-induced dispersion (Davis 1996; Nitsche & Batchelor 1997) could play a role, probably in smoothing out and inhibiting incipient bulges. Given the comprehensive scope of the experiments and calculations already covered by this paper, it seems reasonable to leave a detailed analysis of the tail to the future.

1.6. *Previous work*

What may be regarded as classical experiments with drops of homogeneous liquid undergoing gravitational sedimentation in another miscible liquid – as reported by Thomson & Newall (1885), Kojima *et al.* (1984), Arecchi *et al.* (1989) and Joseph & Renardy (1993) – provide the following observations: As a single drop enters the bulk medium, a tail emanates from the rear. The tail becomes increasingly thinner as the drop continues to fall. A depression region forms at the rear stagnation point; this deepens around the axis of symmetry, progresses to the front, and eventually the

tail is cut off. The drop shape becomes toroidal, and expands in time to a fluid ring, which subsequently disintegrates. Both of the above features of the shape evolution correspond closely to the photographs presented in figures 1 and 2.

Because the drop undergoes a drastic change in configuration, Kojima *et al.* (1984) divided their asymptotic analysis into two parts. In the first part, they dealt with a slightly deformed sphere, and were able to show that, at least for vanishing interfacial tension and inertia, an initially oblate shape develops a rear depression region. Then in the second part they started with a *slender, open* torus, and were able to show that it can expand only if small effects of inertia are incorporated into the analysis. A limitation of their (very reasonable) approach was the absence of a continuous progression from the perturbed spherical shape to a fluid ring. Thus, there was no way to test the seemingly unassailable premise of the open torus – which we now believe not to apply to the insufficiently slender rings for which they reported data (their table III). Our results show that a radial expansion of the torus (and all the other effects as well) are explicable purely within the realm of quasi-static Stokes flow, if the rings are not slender.

The disintegration of the fluid ring and the resultant cascade of fragmentation was first reported by Thomson & Newall (1885), and has ever since been referred to as being caused by the Rayleigh–Taylor instability (Joseph & Renardy 1993, p. 309). This process involves loss of symmetry, fragmentation of drop surfaces, and breakup of membranes spanning the ring, and therefore results in very complex drop geometries (see the experiments of Arecchi *et al.* 1989; and Joseph & Renardy 1993). To the best of our knowledge, nobody has yet presented corresponding calculations.

The interaction of a pair of trailing drops has been the subject of a number of investigations over the past decade. Manga & Stone (1993, 1995) reviewed the existing work, and applied two- and three-dimensional boundary-element simulations to on- and off-axis interactions in systems of two, three and four drops. Their experiments were carried out with air bubbles in corn syrup. Davis (1999) presented a parametric study of axisymmetric two-drop interactions, also computed via boundary elements. The simulations had to stop before actual coalescence.

Adachi, Kiriyama & Koshioka (1978) were the first to report on the behaviour of suspension drops. Their experiments involved swarms of glass particles sedimenting in a glycerol–water solution. They found that, under certain circumstances (mainly low Reynolds number and a large number of particles), the swarm behaved like a roughly spherical drop with a tail. The tail vanished gradually and a hole ran through the swarm along the vertical axis. Then the shape of the drop evolved into a torus, which sometimes broke into pieces. They suggested that breakup of the ring occurred because of inertia, although in their experiments the Reynolds number was considerably smaller than unity. They calculated the instantaneous sedimentation velocity of spherical suspension drops using a swarm of Stokeslets, but did not track the time evolution computationally.

A previously reported set of experiments with sedimentating drops carried out in our laboratory (Schaflinger & Machu 1999) showed a series of phenomena very similar to the observations of Adachi *et al.* (1978).

Substructural effects in gravitational sedimentation of blobs were first specifically considered by Nitsche & Batchelor (1997), who carried out computer simulations of swarms of (up to 320) Stokeslets, along with flow-visualization experiments with coarser, more concentrated suspensions than those used by Adachi *et al.* (1978) or by us. The breakup mechanism they emphasized was the dispersive exodus of particles from a roughly spherical blob in a tail. The term ‘blob’ (rather than ‘suspension drop’)

	Single drop	Interacting drops	Torus	
Liquid drops	E	–	E	Thomson & Newall (1885)
	E + C	–	E + C	Kojima *et al.* (1984)
	E	–	E	Arecchi *et al.* (1989)
	C	–	–	Koh & Leal (1989)
	E	–	–	Koh & Leal (1990)
	C	–	–	Pozrikidis (1990)
	E + C	E	E	Joseph & Renardy (1993)
	E + C	–	–	Stone (1994)
	–	E + C	–	Manga & Stone (1993, 1995)
	–	C	–	Rother *et al.* (1997)
	–	C	–	Cristini *et al.* (1998)
	C	C	–	Davis (1999)
Swarms of particles	E + C	–	E	Adachi *et al.* (1978)
	E + C	–	–	Nitsche & Batchelor (1997)
	E	E	E	Schaflinger & Machu (1999)

TABLE 1. Previous studies of drop deformation in gravitationally-driven flow. E denotes experiments, C denotes calculations.

is appropriate in our terminology, precisely because they were resolving a phenomenon of hydrodynamic dispersion beyond pure hydrodynamics of a continuum pseudo-liquid. But their final model of this substructural effect was of a continuum nature: a correlation for the rate of 'leakage' of particles.

The crucial role of initial conditions in determining the subsequent shape evolution of a suspension drop appears in a number of papers. For example, Kojima *et al.* (1984) mentioned that the drops were splashed onto the free surface of the tank 'in order to facilitate the formation of the ring'. Conversely, Nitsche & Batchelor (1997) noted that a spherical blob was ideal for studying the dispersive leakage of particles in a tail because it is the one shape that maintains a constant form with translation, so that the substructural effect of hydrodynamic dispersion can be isolated from the hydrodynamics of the pseudo-liquid. All of this can be regarded as a general problem of (nonlinear) stability with respect to initial shape. Note that nonlinearity arises from the fact that the drop shape is deformed by the instantaneous (linear) flow field that is, in turn, determined by that very shape.

The review by Stone (1994) summarizes the main results for stability of sedimenting drops. With negligible interfacial tension, infinitesimal perturbations of the spherical shape do not decay: a prolate drop develops a tail whereas an oblate drop forms a cavity and even a ring-like structure (Kojima *et al.* 1984). Interfacial tension moderates the instability so that some finite perturbations revert to the sphere (Koh & Leal 1989, 1990; Pozrikidis 1990). If there are two or more drops, even the spherical shape can be unstable because hydrodynamic interactions will immediately cause deformations (Manga & Stone 1995; Davis 1999). Such effects can be explained using only the far-field disturbances (Manga & Stone 1993).

A main contribution of the present paper is to track 'shape instabilities' far beyond the limits of what has been possible heretofore with boundary-element numerics (Koh & Leal 1989; Pozrikidis 1990; Manga & Stone 1993, 1995; Cristini, Blawzdziewicz & Loewenberg 1998; Davis 1999). In this endeavour the analogy between liquid drops and suspension drops is crucial in developing a simple yet robust computational method. Thus far our calculations are confined to infinite Bond number and unit

viscosity ratio. Changing either of these parameters can produce qualitative changes in behaviour (Pozrikidis 1990; Stone 1994).

Table 1 provides a brief summary of the above literature survey, and points out which stages of drop evolution have been covered by previous investigators using which methods.

The basic problems addressed in this paper are (i) the role of the initial configuration of the drop or drops in determining the formation of the torus, and (ii) the expansion and subsequent breakup of the torus.

2. Theoretical basis and computer simulations

In order to obtain a mechanistic understanding as well as a robust, effective technique for computer simulations, theoretical efforts should address three basic questions: (i) Is there a general, fundamental reason why homogeneously distributed swarms of small, sedimenting particles should (at least in some limit) behave essentially the same as drops of pure liquids? (ii) Can this analogy be exploited in reverse – using simple simulations of swarms of Stokeslets to model flow phenomena of drops that tax and even elude the most sophisticated boundary-element codes? (iii) Are zero-Reynolds-number hydrodynamics alone sufficient (without inertial effects or interfacial tension) to explain the observed phenomena? As will be seen below, all answers are yes.

2.1. *Equations of motion for a swarm of particles*

Consider M spherical particles of equal radius and density sedimenting together in a swarm of characteristic linear dimension R through a Newtonian liquid. As a detailed formulation of the governing equations of motion and underlying assumptions has been given by Nitsche & Batchelor (1997), the following summary can be brief.

For small drop Reynolds number $\mathscr{R}_{\mathrm{d}}$, equation (2), the suspension drop can be modelled using the equations of creeping flow. The crudest representation of hydrodynamic interactions between the particles – applicable at low volume fractions ϕ, for which the ratio ϵ of particle radius to the smallest interparticle distance is small – is to assume that each particle sediments essentially in isolation with the Stokes settling velocity $U_{\mathrm{p}}\boldsymbol{e}_g$ ($\boldsymbol{e}_g$ being a unit vector pointing in the direction of gravity) relative to a local ambient velocity vector that is obtained (at the centre of the particle) by superposing the Stokeslet disturbance fields from all other particles, each of these others being regarded as itself settling in isolation relative to its own local ambient flow. If position coordinates $\boldsymbol{x}$, velocities $\mathrm{d}\boldsymbol{x}/\mathrm{d}t$ and time t are made dimensionless with respect to a, U_{p} and a/U_{p}, we obtain the coupled system of ODEs

$$\frac{\mathrm{d}\boldsymbol{x}_m}{\mathrm{d}t} = \boldsymbol{e}_g + \sum_{n\neq m}(6\pi\boldsymbol{e}_g)\cdot\boldsymbol{F}\,(\boldsymbol{x}_m-\boldsymbol{x}_n), \quad m=1,\ldots,M, \tag{5}$$

where $\boldsymbol{x}_m-\boldsymbol{x}_n$ represents the vector displacement from particle centre n to m, and the tensor field $\boldsymbol{F}$ represents the point-force solution of unit strength (Stokeslet),

$$\boldsymbol{F}(\boldsymbol{x}) = \frac{1}{8\pi r}\,(\boldsymbol{I}+\hat{\boldsymbol{x}}\hat{\boldsymbol{x}}), \quad \hat{\boldsymbol{x}} = r^{-1}\boldsymbol{x}, \quad r=\|\boldsymbol{x}\|. \tag{6}$$

Here $\boldsymbol{I}$ stands for the identity tensor. At this level of approximation the particles appear like point forces; their finite size does not enter the equations. There is nothing to prevent particles approaching each other so closely as to violate the underlying far-field assumption; indeed centres may get closer to each other than the distance

at which their surfaces make contact ($r = 2$). The Stokeslet approximation of the velocity disturbances gives only an $O(1)$ error at $O(1)$ separations $r \geqslant 2$. More serious, however, are the unphysically large fluctuations in velocity that result from numerical overlaps: as the mutually induced disturbance fields (Stokeslets) scale inversely with the separation of centres, arbitrarily large values may be observed in the course of a simulation. Brenner (1999) has pointed out that it is collective far-field effects (not nearest-neighbour interactions) that dominate the trajectories of individual particles in a sedimenting swarm. (This is in contrast to the dynamics of neutrally buoyant suspensions, where care must be taken to resolve the near field and lubrication, as in Stokesian dynamics simulations (Brady & Bossis 1988).) Thus, the only feature of the near field of the Stokeslet that may require correction is the potential for large fluctuations due to overlaps. Any approximation of the disturbance field around a moving sphere that (i) approaches the Stokeslet asymptotically as $r \to \infty$, and (ii) remains of order unity at smaller separations is good enough. Nitsche & Batchelor (1997) avoided the spuriously large fluctuations by preventing the overlaps that cause them with an artificial repulsive potential between the particles. Brenner (1999) did not prevent overlaps, but changed the scalar distance in the Stokeslet,

$$\tilde{r} = \sqrt{r^2 + 1}, \tag{7}$$

so as to eliminate the singularity at $r = 0$. A variation of the latter approach would be to modify the Stokeslet only at distances smaller than some prescribed limit γ:

$$\tilde{\boldsymbol{F}}(\boldsymbol{x}) = \begin{cases} \boldsymbol{F}(\boldsymbol{x}), & r \geqslant \gamma \\ O(\gamma^{-1}), & r < \gamma. \end{cases} \tag{8}$$

The cut-off need not represent the size of the particles ($\gamma = 2$); it need only be of the order of the spacing between centres, which could greatly exceed the particle radius at small volume fractions: $\gamma = O(\phi^{-1/3})$. We mention these refinements mainly for completeness, because our simulations using the unmodified Stokeslet seemed to be unafflicted by inordinately large velocity fluctuations, and gave quantitative agreement with the experiments (§ 4.5). Only in calculating streamlines did we use equation (8), because we might need the velocity too close to where a Stokeslet happens to be sitting. For this purpose we used the simplest provision of turning off the Stokeslet ($\tilde{F} = 0$) at distances closer than the mean interparticle spacing.

The seemingly close correspondence between drops of homogeneous liquids and suspensions noted by previous investigators led Nitsche & Batchelor (1997) to estimate the sedimentation velocity U_b of the whole (spherical) blob of dilute suspension using unit slip velocity relative to the Hadamard–Rybczyński (HR) solution for a liquid drop. In this approximation they neglected both hindered settling and the increase in viscosity over that of clear liquid, both of which effects are first order in ϕ:

$$U_\mathrm{b} \approx \tfrac{6}{5} M\epsilon + 1. \tag{9}$$

The same scaling had been mentioned by Adachi *et al.* (1978). Note that the slip term can be neglected if there are enough particles in the blob. For non-spherical blobs the scaling of U_b is the same; only the pre-factor will change.

If we recast the governing ODEs using R, $M\epsilon$ and $R/(M\epsilon)$ as the characteristic length, velocity and time, respectively, then

$$\frac{\mathrm{d}\boldsymbol{x}_m}{\mathrm{d}t} = (M\epsilon)^{-1}\boldsymbol{e}_g + M^{-1}\sum_{n\neq m}(6\pi\boldsymbol{e}_g)\cdot\boldsymbol{F}(\boldsymbol{x}_m - \boldsymbol{x}_n). \tag{10}$$

It should be noted that

$$(M\epsilon)^{-1} \propto \epsilon^2 \phi^{-1}. \tag{11}$$

Thus, in the limit as the (fixed) excess mass of the suspension is dispersed ever more finely ($\epsilon \to 0$) we can neglect the first term (sedimentation relative to the local ambient flow), and the summation is of order unity. As the modified Stokeslet (8) automatically neutralizes the undefined, discarded term in the summation, we can write

$$\frac{\mathrm{d}\boldsymbol{x}_m}{\mathrm{d}t} \approx \sum_{n \neq m} \left(\frac{6\pi}{M} \boldsymbol{e}_g \right) \cdot \boldsymbol{F}(\boldsymbol{x}_m - \boldsymbol{x}_n) \approx \sum_{n=1}^{M} \left(\frac{6\pi}{M} \boldsymbol{e}_g \right) \cdot \tilde{\boldsymbol{F}}(\boldsymbol{x}_m - \boldsymbol{x}_n). \tag{12}$$

2.2. *The continuum limit*

Let us carry the limiting process of the last section to its logical conclusion, and regard the solids to be so finely dispersed as to constitute a *continuum* of excess mass upon which gravity is pulling downward. Then we can do away with the concept of individual particles and think instead of a body force acting upon what is now a drop of pseudo-liquid. The associated velocity scale is now U_d from equation (2). Using R, U_d and the associated viscous pressure scale, the *inhomogeneous* Stokes equations take the dimensionless form

$$-\nabla p + \nabla^2 \boldsymbol{u} = -\boldsymbol{f}(\boldsymbol{x}) \overset{\text{def}}{=} \begin{cases} -\boldsymbol{e}_g, & \boldsymbol{x} \in \mathscr{V} \\ 0, & \text{otherwise,} \end{cases} \tag{13}$$

where $\mathscr{V}$ denotes that subset of infinite space $\mathscr{V}_\infty$ occupied by the drop of pseudo-liquid. The solution to this inhomogeneous equation can be written in terms of the associated Green's function – which is precisely the Stokeslet:

$$\boldsymbol{u}(\boldsymbol{x}) = \int_{\mathscr{V}_\infty} \boldsymbol{f}(\boldsymbol{y}) \cdot \boldsymbol{F}(\boldsymbol{x} - \boldsymbol{y}) \, \mathrm{d}\mathscr{V}[\boldsymbol{y}] = \int_{\mathscr{V}} \boldsymbol{e}_g \cdot \boldsymbol{F}(\boldsymbol{x} - \boldsymbol{y}) \, \mathrm{d}\mathscr{V}[\boldsymbol{y}]. \tag{14}$$

We can approximate the volume integral according to a simple Monte Carlo method, by summing the integrand (denoted here by $\mathscr{F}$ for short) over a set of randomly distributed points $\boldsymbol{y}_1, \ldots, \boldsymbol{y}_M$. The error of discretization can be estimated from the relevant arithmetic averages (denoted with angle brackets, $\langle \ldots \rangle$) using a standard formula (Press *et al.* 1992, § 7.6):

$$\left\{ \langle \mathscr{F}^2 \rangle - \langle \mathscr{F} \rangle^2 \right\}^{1/2} M^{-1/2}. \tag{15}$$

Because of the weak singularity of the Stokeslet, the prefactor $\{\ldots\}^{1/2}$ increases with M; a numerical test using a spherical drop indicated roughly logarithmic growth, whether the array of sampling points was regular or random. Additional errors from regularizing the Stokeslet according to either formula (7) or (8) are of higher order than the statistical error. Thus we have

$$\boldsymbol{u}(\boldsymbol{x}) = \sum_{m=1}^{M} \left(\frac{V}{M} \boldsymbol{e}_g \right) \cdot \tilde{\boldsymbol{F}}(\boldsymbol{x} - \boldsymbol{y}_m) + O(M^{-1/2} \ln M). \tag{16}$$

According to equation (16), the particle velocities from the ODE system (12) amount to a discrete, Monte Carlo approximation of the integral formula (14).

2.3. *On the equivalence of liquid drops and suspension drops*

We can make a simple observation with important consequences: the volumetric formulation (14) is exactly equivalent to the boundary-integral representation of

the flow field for one or more liquid drops sedimenting under gravity, when the viscosity ratio is unity and the Bond number $\mathscr{B}$ is infinite. Equal viscosities of the drop(s) and surrounding liquid mean that the now-standard boundary-integral equation (Pozrikidis 1990, 1992; Manga & Stone 1993, 1995; Davis 1999) reduces to a simple evolution equation for the velocity vector of the liquid $\boldsymbol{u}(\boldsymbol{x})$ on the interface(s), denoted (collectively) by $\mathscr{A}$,

$$\boldsymbol{u}(\boldsymbol{x}) = \int_{\mathscr{A}} \{\boldsymbol{e}_g \cdot \boldsymbol{y} - \mathscr{B}^{-1}(\nabla_s \cdot \boldsymbol{n}[\boldsymbol{y}])\}\, \boldsymbol{n}[\boldsymbol{y}] \cdot \boldsymbol{F}(\boldsymbol{x}-\boldsymbol{y})\, \mathrm{d}\mathscr{A}[\boldsymbol{y}]; \tag{17}$$

this simplification was exploited by Rallison (1981) and Manga & Stone (1995). Incompressibility of the liquid leads to the following identity for the fundamental solution:

$$\boldsymbol{e}_g \cdot \boldsymbol{F} = \nabla \cdot [(\boldsymbol{e}_g \cdot \boldsymbol{x})\boldsymbol{F}]. \tag{18}$$

Applying this identity together with the divergence theorem to the volumetric formulation (14), we obtain precisely equation (17) with interfacial tension neglected ($\mathscr{B} \to \infty$). In a different context (flow through spatially periodic porous media) Brenner (1980) and Nitsche & Brenner (1989) applied the same identity to a periodic velocity field in order to transfer a volume average within a unit cell to the boundary.

Modulo the $O(M^{-1/2} \ln M)$ discretization error in equation (16), it would seem that the multiparticle problem (12) can be used in place of a boundary-integral formulation to model a liquid drop. To be more precise, this equivalence applies strictly to the quasi-static hydrodynamic equations *at a particular instant* (or in a particular configuration), assuming a statistically uniform distribution of the Stokeslets. Here arises a crucial question: must the distribution of Stokeslets remain statistically uniform upon integrating the ODE system (12) in time? The instantaneous statistical errors might not cancel out, and could then accumulate systematically over time to produce a non-uniform density of points. This is essentially a problem of mixing (Ottino 1989, 1990) – although what we are, in fact, concerned about is the possibility of unmixing. It is only a secondary issue whether the drops are discretized with Stokeslets on the computer or with glass beads in the laboratory. An unusual feature here is that the flow field that sweeps the tracer particles around is generated (via gravity) by the particles themselves. They play the role of active rather than passive tracers, and this subtle ingredient is implicit in the ODE system (12). Our laser light sheet (see § 3, below) could be regarded as illuminating an 'experimental Poincaré section' (Fountain *et al.* 2000); furthermore, particle tracking velocimetry (PTV) has been used to extract Lyapunov exponents (Boffetta *et al.* 2000).

We do not yet have a definitive theoretical argument on the question of statistical uniformity sustained over time, but will offer some compelling *post facto* results in § 4.6, below. On this basis, and drawing from a weighty experimental literature on the correspondence between liquid drops and suspension drops, there is currently no good reason to believe that the flow field produced by a cloud of sedimenting particles should significantly alter their statistical uniformity from the initial condition. Given the already broad coverage of this paper, we confine ourselves to just mentioning the above issue,† and leave a more specifically focused experimental and theoretical investigation to the future. Provisionally, we propose clouds of Stokelets as an advantageous alternative to the boundary-integral formulation for modelling a specific class of drop flows.

The $O(M^{-1/2} \ln M)$ discretization error in equation (16) is formally much poorer

† Thanks are due to an anonymous referee for alerting us.

Set no.	M	δV [m^3] ($\times 10^{-13}$)	R [m] ($\times 10^{-4}$)	a [μm]	$\Delta\rho$ [kg m^{-3}]	ν_f [m^2 s^{-1}] ($\times 10^{-4}$)
C1	6727	3.138	9.178	25	239	1.0
C2	4762	4.363	7.916	25	180	1.0
C3	1902	4.363	5.837	25	180	1.0
C4	4672	5.773	7.865	25	136	1.0
C5	6676	50.35	20.02	25	15.6	1.0
C6	4978	4.363	8.024	25	180	1.0
C7	3000	4.363	5.386	25	180	1.0
C8	15782	4.363	11.34	25	180	1.0
C9	8416	6.545	10.95	25	120	1.0

TABLE 2. Parameter sets for the numerical simulations.

than that for sophisticated implementations of the boundary-element method (Manga & Stone 1995; Cristini *et al.* 1998; Davis 1999). Formal accuracy does not guarantee that no significant cumulative error will creep into a numerical simulation over time. For example Manga & Stone (1993) reported cumulative volumetric errors as large as 5–10% – for extremes of duration, interfacial deformation and viscosity ratio. Our point is that here robustness is more important than accuracy. A simple (if less accurate) Stokeslet simulation can actually survive the twists and turns of fate experienced by sedimenting drops. Such extreme distortions of configuration will either frustrate any method based upon tracking of the interfacial boundary, or else require a very complex grid refinement/redistribution scheme.

Boundary elements have not yet resolved the 'ultimate outcome' of two interacting drops; a typical calculation stops shortly after the entrainment of the trailing drop within the dimple/plume at the rear of the leading drop (Davis 1999, figure 5). The Stokeslet simulations presented in § 4 below reproduce the full sequence of entrainment, coalescence, mixing, and the subsequent cascade of repeated torus formation and breakup that has been observed in our experiments (and those of others) for both liquid drops and suspension drops.

2.4. *Numerical simulations*

The basic task is to integrate the set (12) of $3M$ coupled ODEs numerically. The first step is to distribute particles inside the initial drop shape with the desired (statistically uniform) number density, as set by the volume fraction ϕ or the density difference $\Delta\rho$. A random number generator supplies the Cartesian coordinates of points within a three-dimensional box, and those points lying outside the initial domain are then discarded. The particles are moved sequentially, each over a time step $\delta t_{\max}$ in a flow field determined by all the other particles held fixed in their current positions. A seventh-order Runge–Kutta (RK) routine updates the particle positions, and may take smaller time steps than $\delta t_{\max}$ in the predictor–corrector to converge. (Such a sophisticated integrator is probably not required, but the routine was conveniently at hand.) We did not find it necessary to implement a provision – either equation (7) or (8) – to deal with the singularity of the Stokeslet at $r = 0$: inordinately large velocity fluctuations did not seem to afflict the simulations, as was spot checked using a flag for close approaches. At regular time intervals, numerical snapshots of the particle positions were stored on the hard-disk and analysed later to extract any desired information. Simulations with drop configurations consisting of up to 16 000

particles were carried out, which took considerable computer time (up to 4 weeks in the background) on a 220 MHz Silicon Graphics Origin 200 machine to obtain the cascade of breakups. A test calculation (shown in figure 17) performed with a second-order RK-routine indicated no significant loss of accuracy, but was about ten times faster than the seventh-order scheme. Various parameter sets were used for the numerical simulations, as shown in table 2. The column M gives the discretization for each drop (except set C8), R is the initial radius (and thereby the unit of length displayed in the figures), and a denotes the radius of the particles. In set C8, the total number of particles for both drops is given. The radius listed corresponds to the larger drop (and the unit of length in figure 17), and the smaller drop radius is $0.5R$.

3. Experimental setup

The overall setup for the creation and observation of liquid drops and suspension drops was similar to that used by Schaflinger & Machu (1999), but with more sophisticated optical and electronic equipment, as detailed below.

3.1. *Equipment, materials, and methods of observation*

The dyed liquid or the carefully premixed suspension was injected through a thin needle (inner diameter $d_i = 0.8\,\mathrm{mm}$) via a precisely controllable pump into the quiescent ambient liquid. The transparent tank was built from planar sheets of glass; its inner dimensions were $5\,\mathrm{cm} \times 25\,\mathrm{cm}$ in horizontal cross-section, with a height of 50 cm. The pump was, in principle, comparable to a medical syringe, with a moving piston forcing the desired liquid volume through the needle. The piston was pushed by a threaded spindle of high precision, which itself was driven by a stepping motor. A function generator created a sinusoidal signal and transformed it via an opto-coupling module into the square-wave signal needed to initiate the motor steps. A timing control was employed to produce a series of trailing drops of exact size and at exact time intervals. We used an appropriate sequencer allowing precise and flexible adjustment of both active and passive time intervals within a wide range to switch the power connection of the stepper motor.

Motivated by the similarities between suspension drops (as recorded on video by Schaflinger & Machu 1999) and liquid drops (investigated previously by Arecchi *et al.* 1989; Kojima *et al.* 1984; Joseph & Renardy 1993 and Nitsche & Batchelor 1997) several test series were carried out with the aim of purely flow visualization (e.g. figures 1 and 2). For this paper, video sequences were taken with a SONY DCR-TRV900E 3CCD Progressive Scan Digital Video-Camera, and individual images were captured via appropriate software packages on an APPLE POWER-PC. Besides the detailed PIV-investigations to be described in the next subsection, the shape evolution and the development of the inner flow structure of suspension drops were recorded by means of the PIV-camera and conventional light-sheet techniques. In all experiments, either pure glycerin (density $\rho = 1200\,\mathrm{kg\,m^{-3}}$ and kinematic viscosity $\nu_\mathrm{f} = 10^{-4}\,\mathrm{m^2\,s^{-1}}$) or a glycerin–water mixture was used as the ambient liquid. The suspension drops were made of pure glycerin and a small fraction of glass beads (density $\rho = 2400\,\mathrm{kg\,m^{-3}}$ and mean radius of $a = 25\,\mu\mathrm{m}$) corresponding to volume concentrations of $0.01 < \phi < 0.15$, as determined by the desired density difference $\Delta\rho$. The liquid drops were made out of a mixture of pure glycerine and a small amount of commercial blue ink. To enhance the correspondence between the liquid drops and the suspension drops, the density difference $\Delta\rho$ for the former was adjusted by the amount of water added to the glycerin in the ambient liquid.

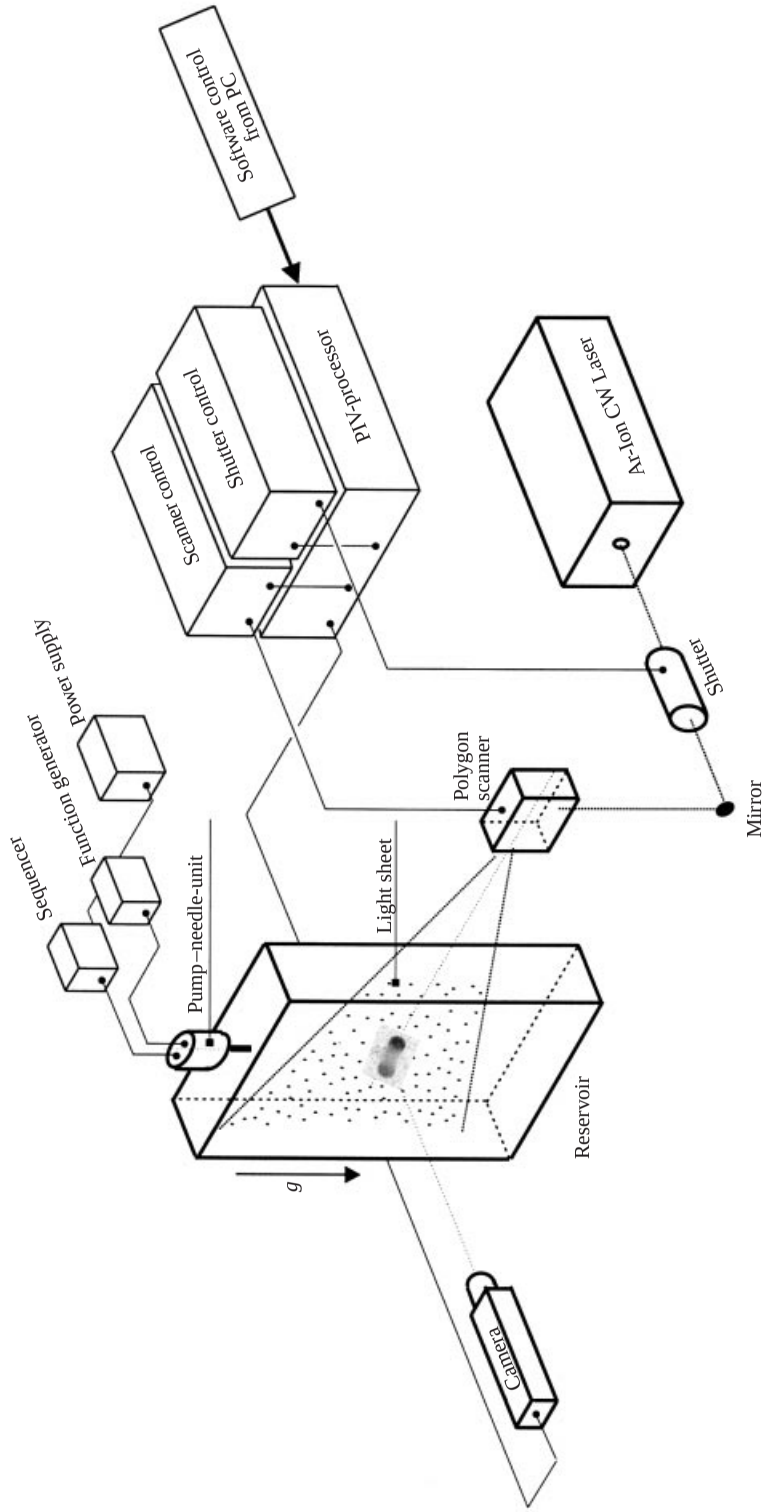

FIGURE 7. Experimental setup, PIV-instrumentation.

3.2. *PIV instrumentation and procedures*

The overall experimental setup is shown schematically in figure 7. The PIV instrumentation setup is a complete system from DANTEC Measurement Technologies. The laser beam is continuously released from a 300 mW argon ion laser and expanded into a light sheet by a 80*X*50 polygon scanner providing a spreading angle of 40°. The individual image pairs were recorded by a 80*C*42 Double-Image 700 cross-correlation camera and the necessary double light pulses were created by a 80*X*41 electro-optical shutter within the beam path between the laser and the light sheet-device. The synchronization of the whole system was controlled by the DANTEC Flow Map PIV-processor in combination with the Flow Manager software package. The raw vector maps were created from the image pairs via the hardware processor. Unavoidable spurious vectors appearing in the raw vector maps were rejected via appropriate validation routines. The subsequent derivation of related quantities from the velocity field was carried out by TECPLOT. The streamlines were determined in a frame of reference relative to the moving drop. For this purpose the settling velocities of the drops were subtracted from the instantaneous velocity fields.

The vertical light sheet was aligned parallel to the reservoir and positioned exactly at the centre of the injection orifice (see figure 7). The camera could be mounted at various distances perpendicular to the light sheet and shifted vertically, retaining the same focal length. Different focal lengths were necessary in order to resolve the motion inside versus outside the drops in more detail. For most of the experiments the solid glass beads served as seeding particles inside the drops; the ambient liquid was seeded with polyamide particles of either 50 μm or 20 μm diameter (depending on the focal length of the camera) to resolve the flow field outside. Due to very intense light scattering, higher concentrations of glass beads within the drop were undesirable when obtaining vector maps. In view of the observed similarities between liquid and suspension drops, the suspension drop could be simulated by using a pure liquid drop with the same density difference, seeded with a suitable volume fraction of polyamide particles. Although this choice would yield better performance of the correlation routines, it also leads to a uniform particle distribution throughout the whole flow field, and particles inside the drop cannot be clearly distinguished in the images. With our emphasis on identifying developing structures inside the drops along with the associated flow field, the optimum seeding requirement was abandoned, and glass beads were retained as suspension particles – but with the volume fraction kept as low as possible. Difficulties related to the determination of streamlines could be ameliorated through the application of the 'average filter' technique to the raw vector maps, thereby smoothing the velocity field.

3.3. *Experimental parameters, composition of drops and liquid*

Depending on whether pure visualization, PIV measurements or both were to be performed during one experiment, the composition of the drops was choosen accordingly for best performance. Other factors being equal, the best results were achieved with the largest drop sizes. The clear visualization of structures and shapes from video-recordings and PIV-images favours a higher volume fraction of glass beads. In contrast, the correlation procedure in PIV (leading from images to vector maps) is usually best for a nearly uniform seeding density. These conflicting requirements militate against simultaneous velocimetry and structural visualization. For this reason, quite different sets of parameters were used during the experiments, as shown in table 3.

The drop radii R given in table 3 represent spherical-equivalent values derived from

Set	ϕ	R [mm]	a [μm]	$\Delta\rho$ [kg m^{-3}]	ν_f [m^2 s^{-1}] ($\times 10^{-4}$)	ν_d [m^2 s^{-1}] ($\times 10^{-4}$)	Corresponding figures	$\mathscr{R}_d = \frac{U_d R}{\nu_f}$
E1	—	3.4	—	20	0.5	1.0	2, 18(*c*)	n.a.
E2	0.04	3.4	25	48	1.0	—	1, 18(*a*, *b*)	n.a.
E3	0.04	2.2	25	48	1.0	—	3	n.a.
E4	0.017	2.7	25	20	1.0	—	4(*a*), 12	0.05
E5	0.013	3.5	25	15.4	1.0	—	8(*a*), 11(*a*), 21, 22	0.07
E6	0.03	2.7	25	35.4	1.0	—	14, 16	0.16
E7	0.15	0.8	25	180	1.0	—	25(*b*)	0.024
E8	0.15	0.6	25	180	1.0	—	—	0.011
E9	0.013	2.0	25	15.6	1.0	—	25(*d*)	0.031

TABLE 3. Parameter sets of the experiments.

the injected volume. As mentioned earlier, a denotes the mean radius of the glass particles. Due to the low volume fractions, the viscosity of the suspension drops does not deviate significantly from that of the ambient liquid: essentially unit viscosity ratio is implied for all parameter sets (E2–E9) related to suspension drops. Parameter set E1 corresponds to a pure liquid drop with viscosity different from the ambient liquid. The tabulated Reynolds numbers $\mathscr{R}_d$ (based upon the radii R and settling velocities U_d) indicate the order of magnitude for each set of parameters, but were not evaluated at the individual stages. Experiments with sets E1–E3 were conducted for the purpose of purely visualization, and so precise settling velocities (and hence the corresponding Reynolds numbers) are not available. For single drops (sets E4 and E5), U_d was evaluated during one of the initial stages where a nearly spherical shape prevailed. In the case of pairs of drops (sets E6–E9) an average velocity was determined from the recordings between one stage where the drops are still clearly distinguishable and the stage where they have mixed. It should be emphasized that the parameters specified in table 3 are values according to the composition of the premixed suspension. The actual composition of the individual drops may slightly deviate from these values due to unavoidable settling during the period of manipulation before injection. Furthermore, the injected volume is controlled by the stepping motor with an uncertainty of $\pm$one step and the associated volume in the barrel of the syringe. In most cases the volume of the drop was equivalent to several hundred steps, so that the uncertainty in radius was effectively negligible. However, the experiments for very small drops (at higher volume fractions to match the number densities used in the computer simulations) approached the lower size limit of the setup. The radii tabulated for parameter set E7 (7 motor steps) and particularly E8 (3 motor steps) therefore represent only nominal values, but could have differed between various experimental runs. It should be mentioned here that the experiments with parameter set E8 exhibited noticeably different settling velocities between different runs.

4. Numerical solutions and experimental measurements

In this section we compare computer simulations from § 2 with the experimental results obtained according to § 3. The material is organized in the same order as the introduction, starting with initial configurations for single drops, then proceeding

Phenomenon	Agreement between theory and experiment
Sedimentation velocity	Quantitative (microscopic and macroscopic)
Initial entrainment of clear liquid	Qualitative
Point of disconnection of the tail	Quantitative (macroscopic)
Coalescence and mixing	Quantitative (microscopic and macroscopic)
Formation of closed torus	Qualitative
Transition to open torus and cascade of breakups	Qualitative
Bulging and breakup of the tail	Qualitative

TABLE 4. Demonstrated level of agreement between computer simulations of swarms of Stokeslets and experiments on suspension drops.

to pairs of interacting drops. Finally, we discuss the transition from the closed torus to the open torus, and the subsequent cascade of disintegrations. As was the case in § 1.4, all streamlines to be presented below correspond to a reference frame moving with the drop, and to a meridian plane (in the axisymmetric case), or at least a sectional plane of reflective symmetry. Beyond the close qualitative agreement – for configurations and streamlines – between computer simulations and experiments, quantitative comparisons of the configurational evolutions were made by matching parameters (as nearly as possible) on two levels: *macroscopic* (dimensionless) versus *microscopic* (dimensional). In the latter case the swarm of Stokeslets was essentially a literal model of the suspension drop in the laboratory. Agreement between macroscopic or dimensionless parameters for different but corresponding microscopic realizations (whether experimental or theoretical) justifies viewing the swarm of particles as a continuum pseudo-liquid. The categories of the various results are summarized in table 4.

4.1. *Effect of initial shape on subsequent evolution*

As mentioned in § 1.6, Nitsche & Batchelor (1997) found that an initially spherical blob does not substantially change its shape when falling through an infinite expanse of lighter liquid. They reported that the envelope of closed streamlines is a spherical surface lying slightly inside the (fuzzy) boundary of the blob. Particles lying outside that surface get swept to the rear and are lost from the collective to form a tail. The interaction of the tail with the blob proved to be too weak to significantly alter the blob shape. Clearly, no outer liquid is entrained by the blob. We confirmed these findings with calculations using a much finer discretization of 4978 particles (parameter set C6). Experimental trials showed that a perfectly spherical drop without interfacial tension is essentially impossible to produce in the laboratory, and that those shapes that do actually occur develop into a torus. Figure 8(*b*) shows the envelope of closed streamlines calculated for a bell shape (a cone on top of a hemisphere) similar to those obtained by the injection process in the laboratory; see figures 8(*a*) and 11(*a*). There are two important features. First, some streamlines cut through the surface of the drop at the rear, thereby entraining liquid, sweeping out particles from the centre, and forming the ring. Second, the drop extends at least partly outside the envelope toward the front or sides, and the associated particles are swept to the rear by the liquid passing by, causing the coaxial tail. The second mechanism is also operative in the case of a spherical blob (Nitsche & Batchelor 1997). The relation of the stream envelope to the shape of a drop is explored in figure 9 where two new

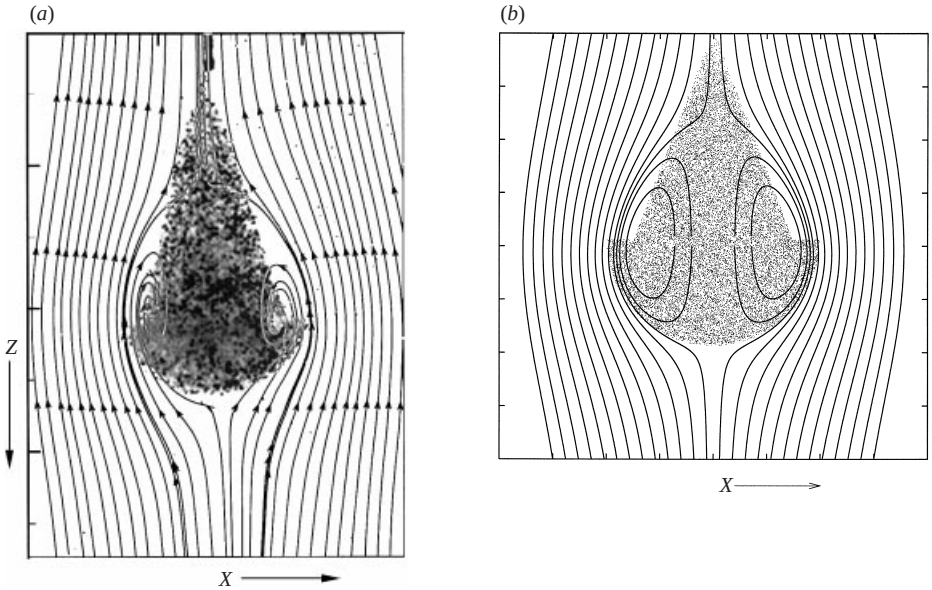

FIGURE 8. Instantaneous streamlines for the bell-shaped drop. The streamlines at the rear which cross the boundary of the drop are responsible for the entrainment of pure liquid. (*a*) PIV measurements, parameter set E5 (table 3), distance between major tickmarks corresponds to 5 mm; refer to the first photograph of figure 11(*a*). (*b*) Streamlines for a bell shape (a cone on top of a hemisphere), calculated using 60 000 randomly distributed Stokeslets.

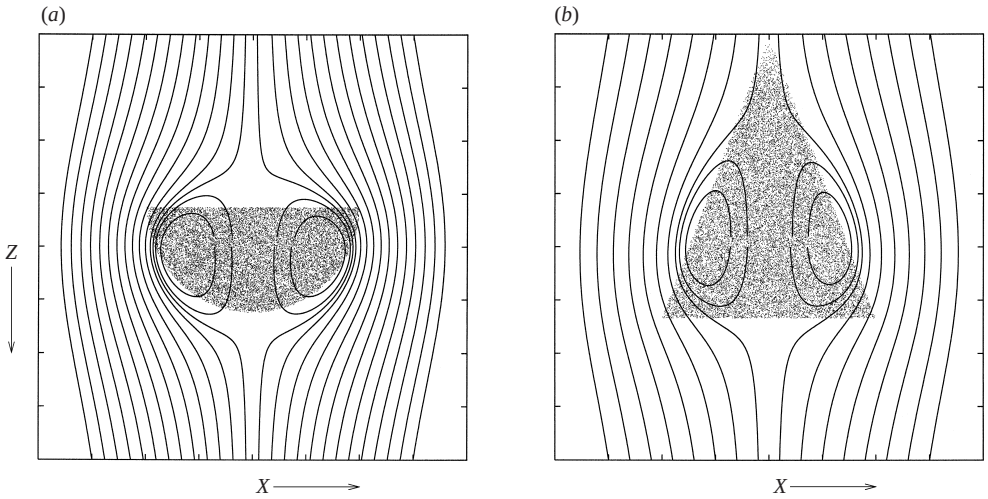

FIGURE 9. Streamlines for different shapes of suspension drops: (*a*) hemisphere; (*b*) cone.

shapes (hemispherical and conical) are presented for comparison with the bell-shaped drop. Both of them also illustrate the basic mechanism identified above.

Figure 10 shows the time evolution of a bell-shaped drop in a meridian plane (with dimensionless units), calculated using parameter set C1 from table 2 and a time step input of $\delta t_{\max} = 0.043$ to the RK-routine. The configurations represent snapshots taken at dimensionless time intervals $\Delta t = 4.3$ (i.e. every 100 time steps), and each new configuration is shifted 4 units to the right. To visualize the velocity scale, we also

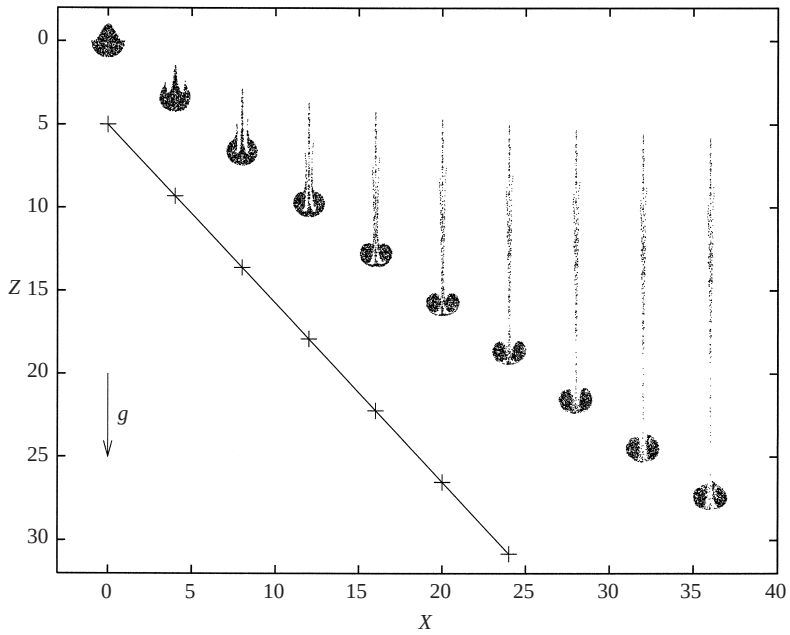

FIGURE 10. Evolution of a bell-shaped drop, calculated using parameter set C1 (table 2). Drop position is shifted four units to the right at each dimensionless time interval $\Delta t = 4.3$.

plot the HR solution for a perfectly spherical drop of the same density difference and the same occupied volume per particle δV. As can be seen from the second image in figure 10, surrounding liquid is entrained at the rear (upper) part of the drop, which progresses to the front stagnation point (images 3–5). Due to the spherical vortex the liquid is carried back to the rear and forms a spike. The tail is left behind and in time the shape becomes toroidal. Another feature of the early stages of evolution is the formation of a secondary coaxial tail surrounding the initial spike. This tail is also visible in the experiments and indicates the process of entrainment.

In view of the mechanism described above, there remains the question of why the blobs observed experimentally by Nitsche & Batchelor (1997) did *not* form a torus. We can speculate on several reasons. First, their blob Reynolds number was not small. Second, their tank was not high enough to observe the transition from blob to torus. (According to our calculations, figure 10, the drop must move through approximately 30 radii to form a ring.) Third, their blobs did not conform to our assumptions of small volume fraction and fine discretization. The coarseness of the discretization alone seems to be enough to prevent the formation of a torus. This last conclusion is now confirmed by a simulation (not shown here) with only 300 particles starting from a hemispherical shape. In contrast to the behaviour for a fine discretization of the same shape, the coarse (hemispherical) blob did not entrain liquid and develop into a torus – because of some substructural effect such as hydrodynamic dispersion.

4.2. *A model for the formation of the initial drop shape observed in the experiments*

In order to avoid arbitrarily chosen initial drop shapes, figures 8(*b*) and 10, we also wanted to model the drop injection process (until now the starting point for the simulations) within the premise of a swarm of Stokeslets. We implemented a simple method which did not require significant changes in the computer code. A swarm

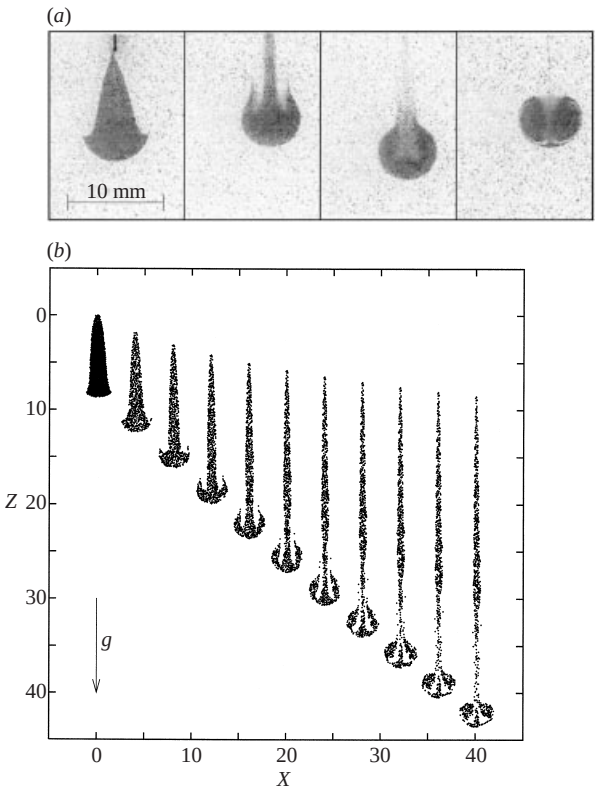

FIGURE 11. Shape evolution of the laminar jet in a meridian plane after the injection process has stopped. (*a*) Light-sheet pictures from experiment with parameter set E5 (table 3), the sequence is continued in figure 21. (*b*) Numerical simulation using parameter set C4 (table 2). Drop positions are shifted 4 units to the right at each time interval $\Delta t = 2.36$ s.

of the given number M of Stokeslets is confined geometrically within the interior of a cylinder that represents a virtual syringe sticking into the liquid (but we do not explicitly consider the solid walls of a real syringe, which would have a hydrodynamic effect). Over a number of time steps the suspension is moved downward with the desired injection velocity. Every particle that crosses the mouth of the (virtual) needle is assigned a vector strength that corresponds to the momentum of the jet; at that point it enters the simulation. As soon as it moves away from the mouth, it is reassigned a Stokeslet strength corresponding to the drag of an isolated particle settling under gravity. When all of the Stokeslets have entered the liquid, the simulation proceeds as described in § 2. We note that there is no simple *a priori* relation between the volume fraction of the drop at the end of the virtual injection process and the initial volume fraction within the virtual syringe.

Figure 11(*b*) shows the time evolution starting with a drop produced by our virtual injection process, calculated with the parameter set C4 from table 2 and the (dimensional) time step $\delta t_{\max} = 0.01$ s. The initial image agrees very well with our experimental observations, figure 11(*a*). No reference HR trajectory is plotted because, as mentioned before, the volume fraction of particles in the initial drop is not known accurately.

It is interesting to note that, despite a difference in the initial shape, the evolution is qualitatively very similar to that shown in figure 10 for the arbitrarily chosen bell

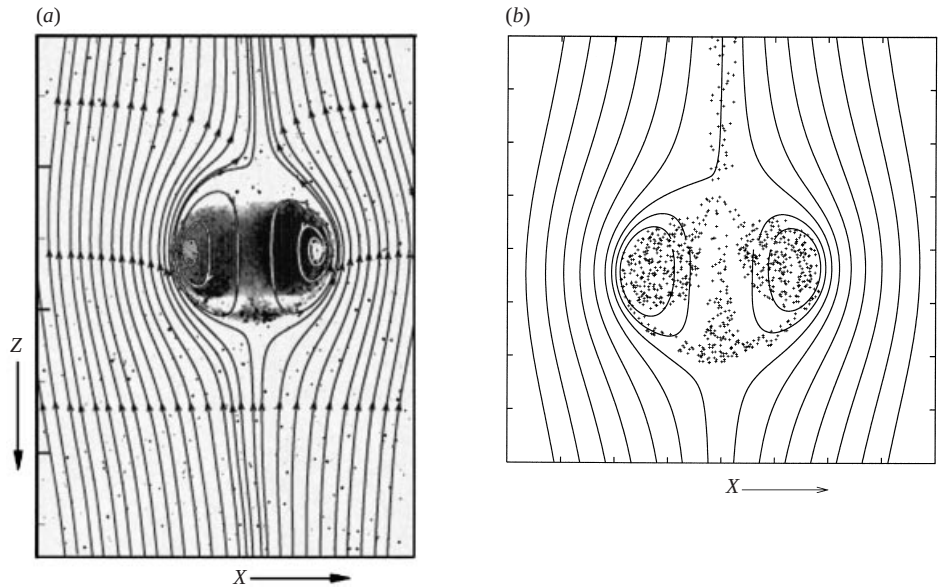

FIGURE 12. Streamlines for the mushroom-shaped drop: (*a*) PIV measurements, parameter set E4 (table 3), distance between major tickmarks corresponds to 5 mm; (*b*) the simulation exhibited in figure 11. Note that the rear stagnation point is situated significantly outside the drop boundary which causes the tail to become disconnected. Drop (*a*) is similar to the last photograph in figure 11(*a*), and in (*b*) the last drop of figure 11(*b*) is shown.

shape. Figure 12 compares PIV streamlines for a real (mushroom-shaped) drop, the rightmost photograph in figure 11(*a*), with calculated streamlines for the last image in figure 11(*b*). Obviously, the numerical discretization is much coarser than the number of particles in the actual experiment, but the streamlines are very similar.

4.3. *Pairs of interacting drops*

As has been shown above, a swarm of Stokeslets contains the physical information necessary to explain essentially all of the phenomena observed in the laboratory for a single drop. The advantage of a Stokeslet simulation is that the computation can be extended to two or more drops without any conceptual extension of the method. Therefore we calculated the interaction of both vertically aligned (axisymmetric) and horizontally displaced drops. Figure 13 combines (dimensionless) configurational evolutions for two independent simulations of axisymmetric trailing drops. Snapshots of the swarms of Stokeslets are shown in pairs in an X,Z projection, the left and right images of each pair corresponding to the respective parameter sets C5 and C2 from table 2. The former images include all particles, whereas the latter are sectional views, including only particles lying within a thin slice straddling the meridian plane. Successive snapshots, separated by the dimensionless time interval $\Delta t = 1.84$ are shifted 10 units to the right ($+X$-direction). Although the parameter sets are completely different, the configurational evolutions collapse onto each other when viewed on a dimensionless basis – a result that is corroborated by the experiments; see §4.5 below, especially figure 25. Thus, flow visualization and PIV streamlines for larger drops (which are more advantageous for the experiments) can be used to check Stokeslet simulations using fewer particles, assuming that the Reynolds number is much smaller than unity.

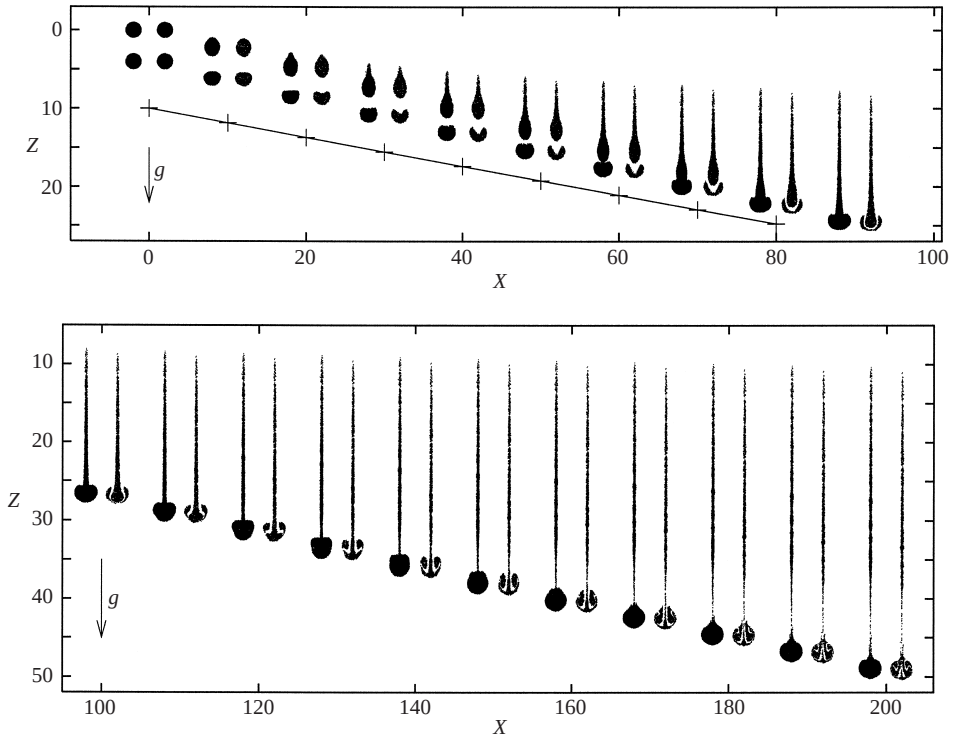

FIGURE 13. The interaction of axisymmetric trailing droplets. Two independent simulations are exhibited at each instant. It shows that the scale of evolution in dimensionless form does not depend on the drop properties. Parameter set C5 (table 2) is used for the drops shown in a (X/Z) projection (each left-hand configuration). Parameter set C2 is used for the drops shown in a meridian plane (each right-hand configuration). Drop positions of both simulations are shifted ten units to the right at each dimensionless time interval of $\Delta t = 1.84$. A HR trajectory for a single drop of unit radius is drawn as a reference scale.

Figure 15 below displays the calculated evolution (parameter set C2 in table 2, time step $\delta t_{\max} = 0.03$) for two horizontally displaced drops in a sectional plane of mirror symmetry. At regular dimensionless time intervals $\Delta t = 1.84$ the positions of both drops are shifted 4 units to the right. The horizontal offset of the initial configuration is 2 radii. Again the HR trajectory sets the velocity scale.

From the beginning, the trailing (upper) drop in figure 13 becomes highly elongated and forms a long tail. It catches up with the leading (lower) drop and pokes through, as reported by Manga & Stone (1993). The toroidal vortex causes both drops to mix, until the interface becomes so convoluted that one cannot distinguish one drop from the other, and the tail becomes disconnected and is left behind. These are precisely the experimental observations displayed in figure 14. The case of horizontally displaced drops (figures 15 and 16) reveals the effect explained by Manga & Stone (1993) that the trailing drop moves into vertical alignment with the leading drop. The subsequent process of catching up and mixing with the leading drop is similar to the axisymmetric case (figure 13). Both cases produce an essentially spherical compound drop, which eventually forms a torus that breaks up in time. In the case of finite Bond number, the same stages of a phenomenon called 'pass-through' – identified in Kushner, Rother & Davis (2001) – appear similar to the closing stages in figure 15. If pass-through occurs repeatedly, it is vaguely analogous to the mixing of our miscible drops.

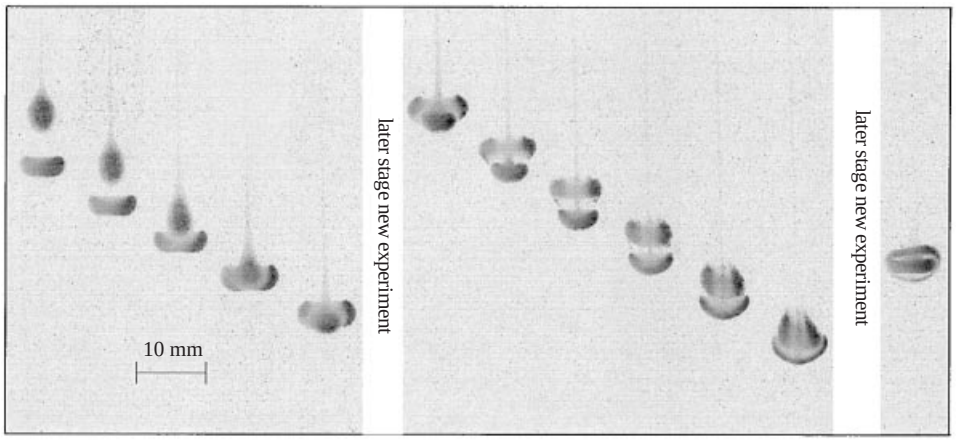

FIGURE 14. The interaction of two vertically aligned suspension drops in a meridian plane illuminated by a laser light sheet. Experiment with parameter set E6 (table 3).

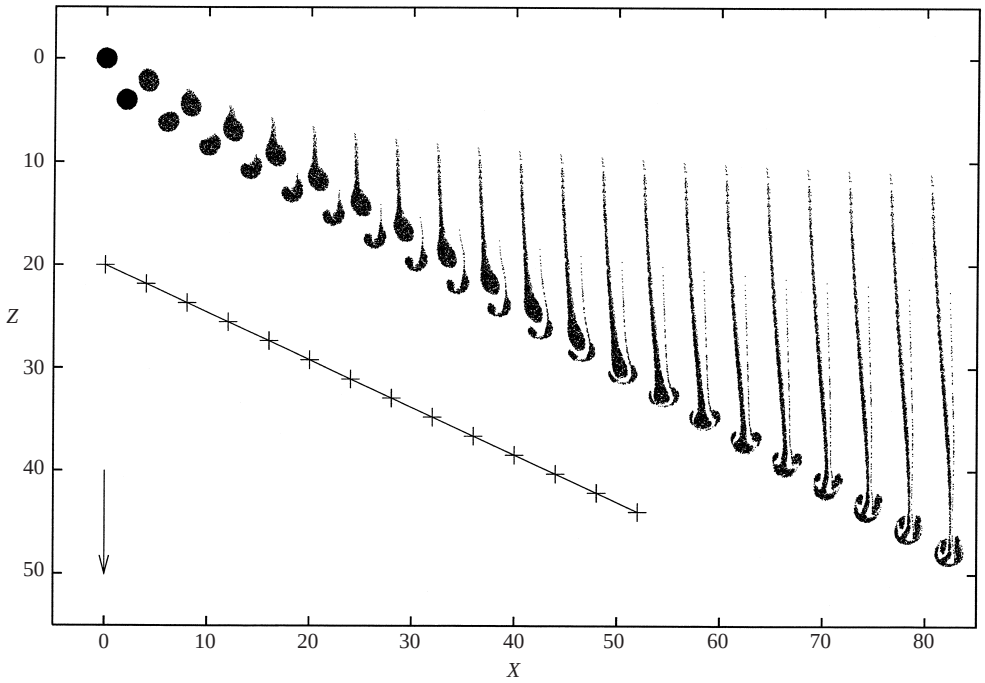

FIGURE 15. The interaction of two horizontally offset suspension drops in a sectional plane. Parameter set C2 (table 2) is used. Drop positions are shifted four units to the right at each dimensionless time interval of $\Delta t = 1.84$. A HR trajectory for a single drop of unit radius is drawn as a reference scale.

The evolution of two buoyant, axisymmetric trailing drops of different size is displayed in figure 17. It is a reproduction of the left-hand configuration of figure 3 in the paper of Manga & Stone (1993) (unit viscosity ratio and infinite Bond number). The scaling of these authors differs by a factor of 4/15 from our scaling (HR-scaling), thus explicit times are exhibited for the sake of comparison in our figure 17. This case served as a reference for the numerical code in two ways: (i) only a second-order RK routine was used, showing essentially no loss of accuracy as compared to the seventh-

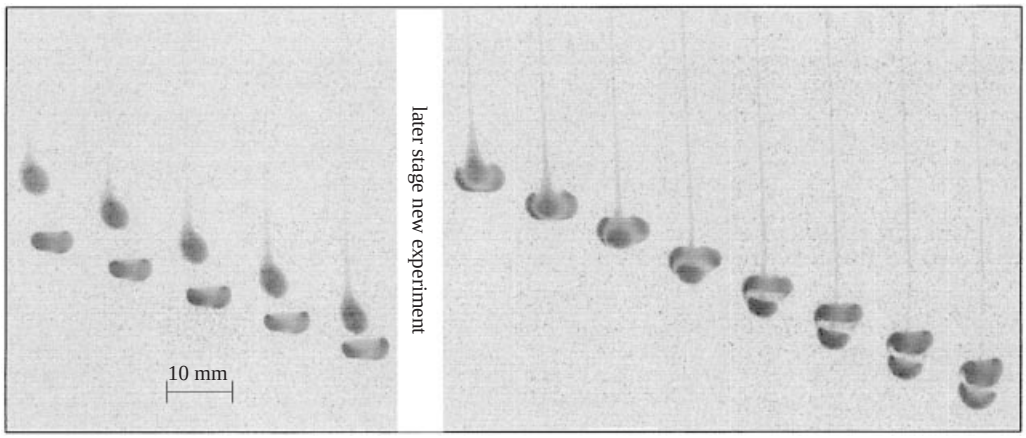

FIGURE 16. The interaction of two horizontally offset suspension drops in a sectional plane illuminated by a laser light sheet. Experiment with parameter set E6 (table 3).

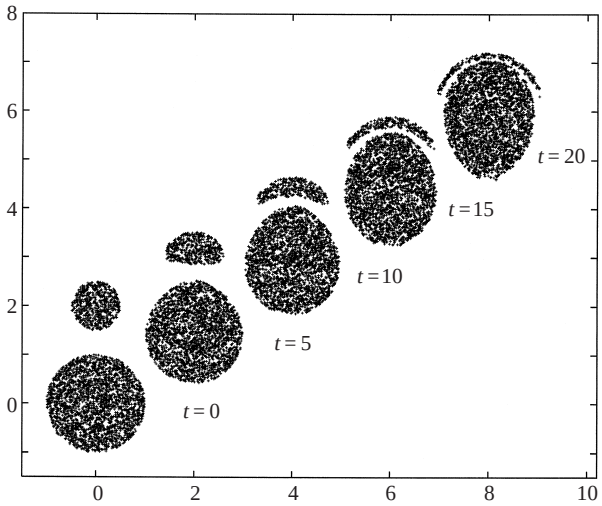

FIGURE 17. The interaction of buoyant axisymmetric trailing droplets of different size. The left-hand evolution of figure 3 of Manga & Stone (1993) is reproduced, the dimensionless times displayed are calculated accordingly. Both drops are shifted two units to the right at each dimensionless time interval of $\Delta t = 5$. The larger drop has twice the radius of the smaller drop.

order scheme used for all the other simulations, and (ii) it is in complete agreement (regarding both location and time of specific configurations) with the results of Manga & Stone, thereby confirming the applicability of a Stokeslet simulation for this class of flows.

4.4. *Transition from the closed to the open torus, and cascade of ring disintegrations*

As mentioned in § 1.4, there is an envelope of closed streamlines that extends beyond the boundary of the fluid ring – hence the term closed torus. The closed torus undergoes a series of cyclic expansions and contractions, with expansion finally prevailing. The larger torus that finally emerges is actually an open torus, and is unstable. The streamline patterns for the closed versus open tori are clearly distinguishable in the simulations, figure 24.

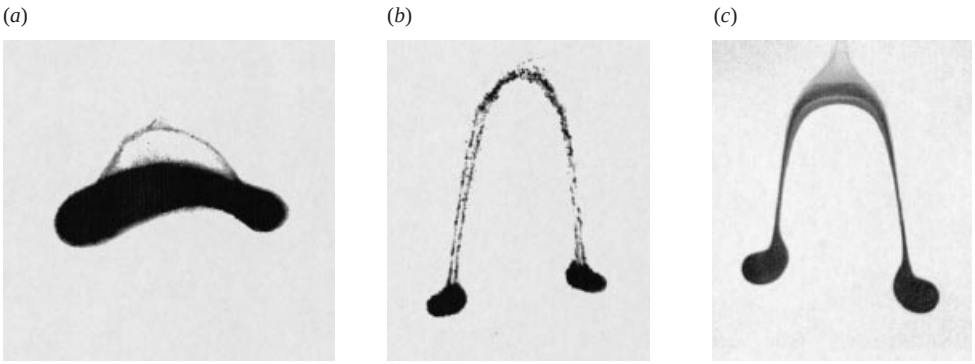

FIGURE 18. (*a*) The open torus is spanned by a membrane of particles (parameter set E2 in table 3). (*b*) The open torus formed from a suspension drop becomes unstable and breaks into two secondary droplets (parameter set E2 in table 3). (*c*) Same as (*b*), but for a liquid drop, (parameter set E1 in table 3). Photographs were captured from a video.

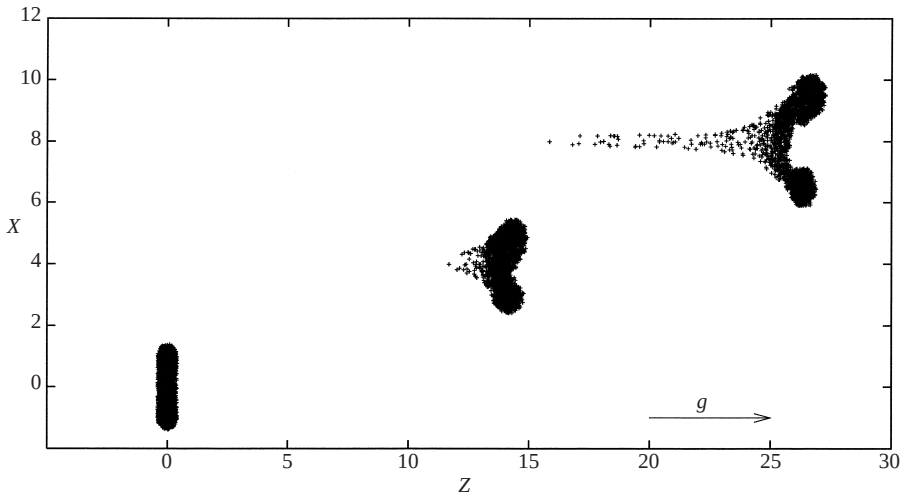

FIGURE 19. Time evolution of an initially open torus in a (Z/X) diagram. The radius ratio (cross-section/ring) is 0.4. Streamlines for a slightly fatter torus (radius ratio 0.5) appear in figure 5. The graph is turned 90° counterclockwise to make it compact. Parameter set C7 from table 2 is used.

Occasionally, during the transition from the closed torus to the open torus, a membrane spans the fluid ring, as shown in figure 18(*a*). Subsequently bulges form around the open torus, and it breaks into two or three secondary droplets, as shown in figure 18(*b*). A corresponding stage for a liquid drop appears in figure 18(*c*); see Joseph & Renardy (1993). If one starts the simulation from a perfectly symmetric, open torus, then the torus elongates and breaks apart. Figures 19 and 20 show such behaviour in non-slender versus slender cases.

In their experiments (at effectively zero Reynolds number) Kojima *et al.* (1984) observed a monotonically expanding torus, which they could not account for in their asymptotic theory of the slender open torus without including additional inertial effects. We suspect, however, that a closed torus was actually present in their experiments, and that it was mistaken for an open torus in the absence of available streamlines.

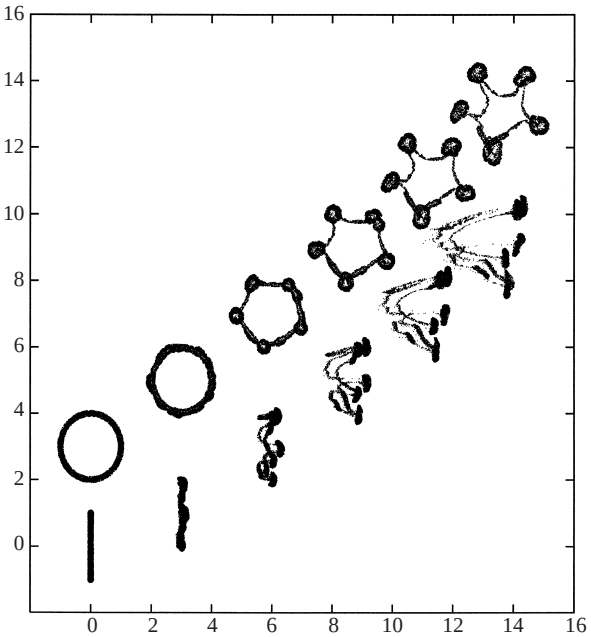

FIGURE 20. Breakup of a slender torus (radius ratio 0.1), viewed from top and from the side. Parameter set C9 from table 2 is used.

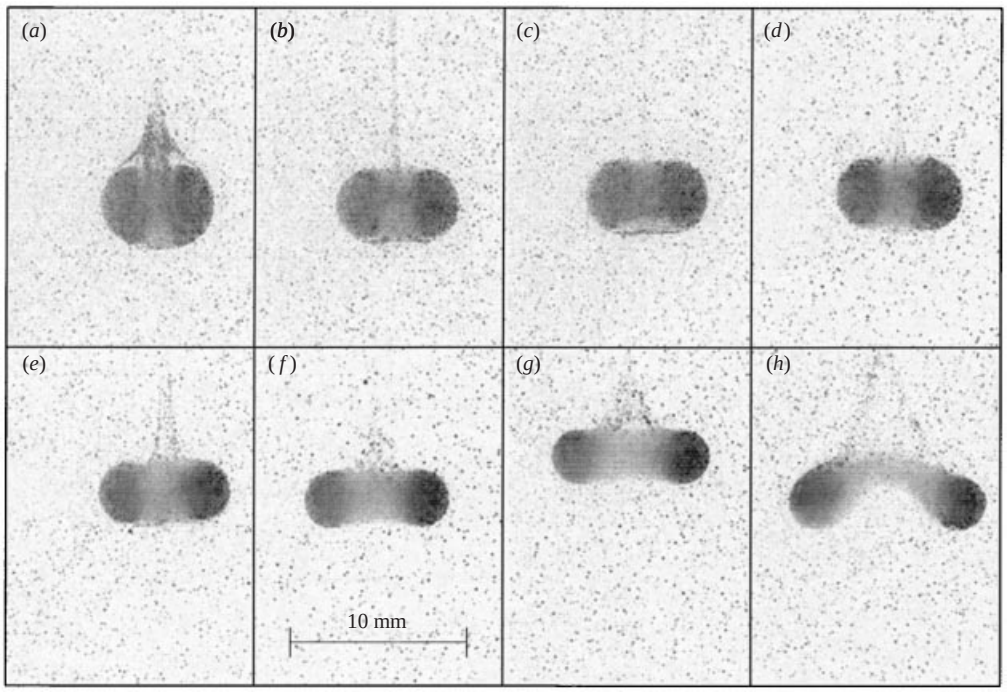

FIGURE 21. Further shape evolution of a single drop, closed torus and transition to an open torus: light-sheet pictures from experiment with parameter set E5 (table 3). This sequence continues from figure 11(*a*).

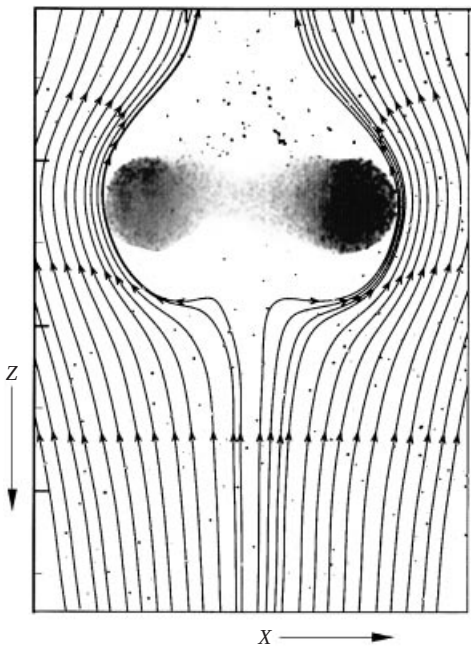

FIGURE 22. Streamline pattern for a closed torus just before the transition to an open torus begins; parameter set E5 (table 3), distance between major tickmarks corresponds to 5 mm; refer to figure 21(*g*).

Figure 21 shows the shape evolution for a single drop illuminated in a meridian plane by a laser light sheet. This set of images continues the sequence started in figure 11(*a*). The first six photographs clearly display the evolution of a closed torus from the mushroom-like drop depicted in the picture at the far right in figure 11(*a*). Streamlines for figure 21(*g*) appear in figure 22. Special attention should be focused on figure 21(*g*, *h*), where the change from a closed torus to an open torus can be identified.

The disintegration described above is actually the first in a series of disintegrations. Figure 23 shows the later stages of a numerical simulation (parameter set C3 in table 2, $\delta t_{\max} = 0.01$) that progressed from two identical axisymmetric trailing drops of unit radius, to a compound drop, to a closed torus, to an open torus, and a disintegrating fluid ring. As before, the velocity scale is set visually by the HR trajectory for a drop of unit radius. The numerics (figure 24) precisely reproduce the cascade of breakups known from our experiments and earlier observations (Thomson & Newall 1885; Arecchi *et al.* 1989). After the compound drop has formed, it must settle through roughly 185 initial radii to start the cascade process. However, to form the tertiary droplets it takes only 35 initial radii from the secondary droplets.

Figure 21(*g*, *h*) corresponds closely to the numerically determined shapes marked with (+) and (*), respectively, in figure 23. The torus in figure 21(*g*) corresponds to the streamline pattern shown in figure 22. There is a closed streamline envelope, with only the upstream stagnation point being visible in the picture. Figure 21(*h*) shows the formation of bulges, indicating the breakup of the ring. In this case a reasonable streamline pattern could not be extracted from the PIV experiment because of the three-dimensional nature of the flow field.

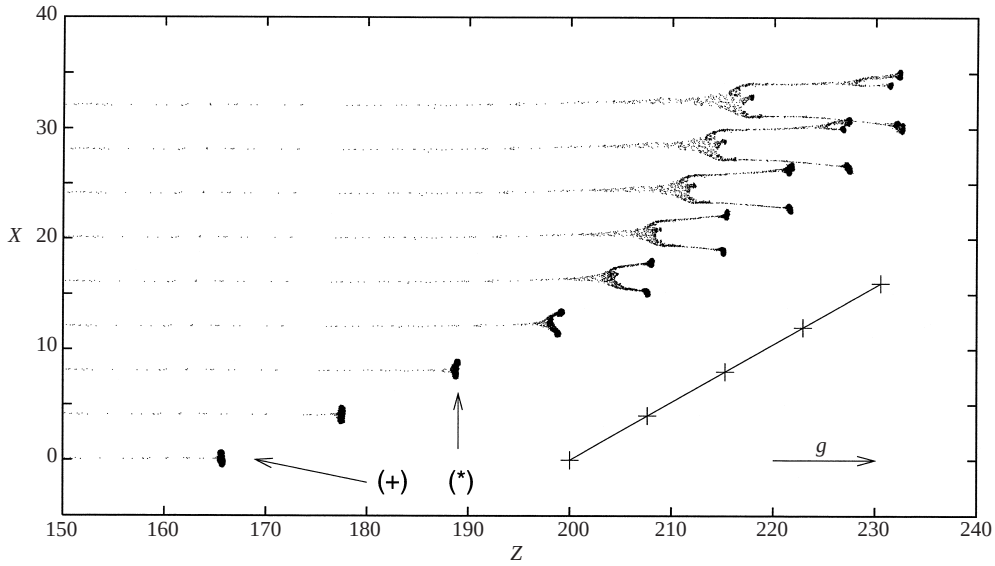

FIGURE 23. The cascade of ring disintegration in a (Z/X) diagram. Drop positions are shifted 4 units in x at each dimensionless time interval of $\Delta t = 7.64$, parameter set C3. The graph is turned 90° counterclockwise from the vertical to make it compact.

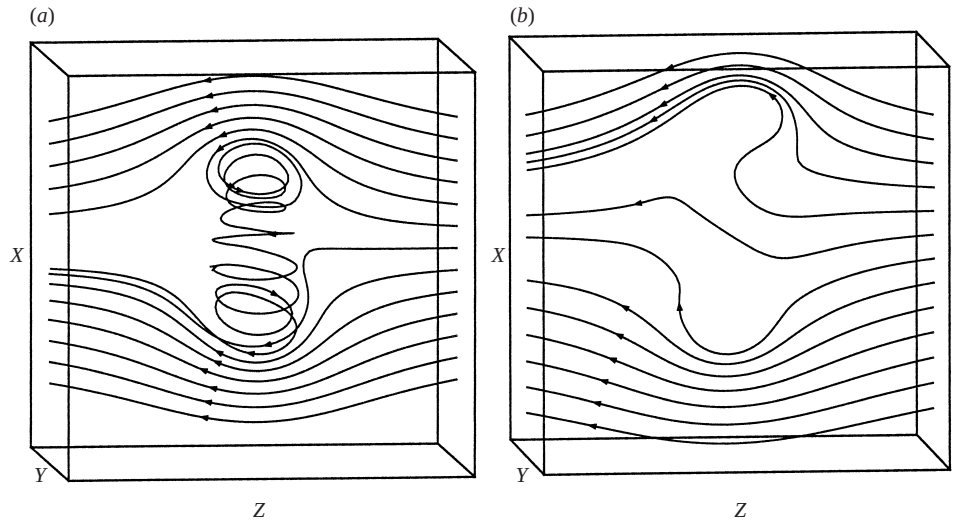

FIGURE 24. Three-dimensional streamlines for the marked tori in the computer simulated progression of figure 23. In each case the ring-like swarm of Stokeslets (omitted for clarity of the streamlines) is centred within the cubical volume shown. The streamlines start along a regular spacing at a line parallel to the X-axis in a sectional plane which intersects the centre of the torus. (*a*) Closed torus = (+); (*b*) open torus = (*).

4.5. *Quantitative comparison of computer simulations and experiments*

As has been observed above in §4.3 (figure 13), the macroscopic configurational evolutions for different swarms of Stokeslets collapse onto each other when they are presented in dimensionless space and time variables. Beyond confirming this general conclusion of scaling in the laboratory, we also carried out experiments that

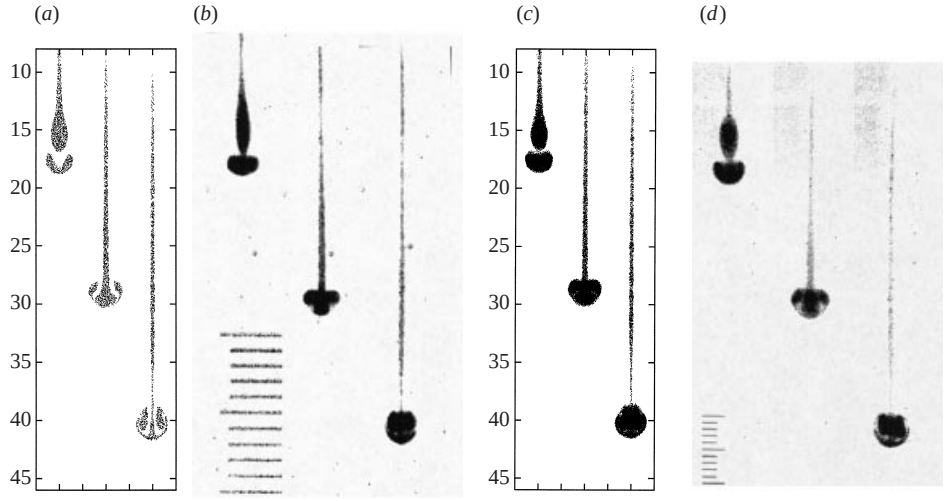

FIGURE 25. Quantitative comparison of computer simulations and experiments. (*a*) Computed drop positions in a sectional plane (parameter set C2 in table 2), $\Delta t = 9.2$ (equivalent to 3 s). (*b*) Corresponding photographs of drop positions from an experiment (same parameters, set E7 in table 3). (*c*) X/Z projection of computed drop positions (parameter set C5), $\Delta t = 9.2$ (equivalent to 13.5 s). (*d*) Corresponding photographs of drop positions from an experiment with the same parameters, set E9 in table 3. The scale bar in (*b*) and (*d*) shows 10 mm.

matched the microscopic parameters in the computer simulations. The comparison was complicated by the narrow range of overlap between the computationally versus experimentally accessible parameters. The number of particles used in the simulations represents the upper limit of our computational capability (SGI Origin 200). But the same parameters in an experiment carry our setup to the lower limit of performance (see § 3.3). As a demanding example, we used axisymmetric trailing drops – a case in which the early evolution is determined mainly by the interactions between the drops, the initial shapes being only of secondary importance; see § 1.3. This is important, because the spherical drops assumed for the initial condition in the computer simulations cannot be reproduced in the laboratory, in the absence of interfacial tension. In figures 25(*a*) and 25(*c*), three stages of evolution calculated using parameter sets C2 (*a*) and C5 (*c*) from table 2 are compared with equivalent photographs corresponding to the respective experimental parameter sets E7 (figure 25*b*) and E9 (figure 25*d*) from table 3. The successive images in parts (*a*) and (*c*) are a subset of those appearing in figure 13, and are separated by the dimensionless time interval $\Delta t = 9.2$. The equivalent dimensional time intervals in (*b*) and (*d*) are 3 s (75 frames of the video camera) and 13.52 s (338 frames), respectively. For the computed images in (*a*) and (*c*), the pixel size does not represent the real dimension of the particles, so the inner structures in (*c*) are not clearly discernible. This limitation does not affect the photographs. The difference in the lengths of the scale bars in (*b*) and (*d*), both indicating 10 mm, reflect different distances of the camera from the tank.

Despite the different initial drop shapes, agreement between simulated and actual configurations is strikingly good for both pairs of parameter sets: there is a close match for both the times and the locations at which distinct configurations appear, as far as can be discerned from the gross shapes. (Substantially more difficult would be a very detailed, quantitative analysis and comparison of the internal structures, which is left to the future.) This result validates the use of Stokeslets, with no correction

for near-field interactions. Furthermore, the fact that different numbers of particles (whether Stokeslets or glass beads) collapse onto the same macroscopic configurations at corresponding dimensionless times indicates that the fineness of our discretization is sufficient to yield continuum pseudo-liquid behaviour. In other words, one can neglect substructural effects such as hydrodynamic dispersion, which are associated with coarseness of a blob (Nitsche & Batchelor 1997).

The measured settling velocities of the trailing drop in figure 25(b, d) were 2.3% and 8.9% smaller, respectively, than the computed velocities in (a, c), which may be explained by hydrodynamic effects of the sidewalls. In a further comparison of parameter sets C3 and E8, the measured settling velocity exceeded the calculated value by 2.3%. But the very small size of the drop pushed the capabilities of our experimental setup, with $\pm 33\%$ uncertainty in the injected volume; see also § 3.3. Thus, images are not shown for this case.

One feature was not predicted with consistent, quantitative accuracy by the computer simulations: the distance travelled before the onset of the cascade of breakups (figure 23). The reason lies in the irreproducibility of this distance in the physical system itself. In other words, although exceedingly fine details do not alter the qualitative macroscopic behaviour, they do affect this specific quantitative outcome. In some of the experiments the breakup started at a distance of about 200 initial radii from the injection needle; in other cases the torus reached the bottom of the tank without yet showing any sign of breakup.

Two effects compounded the variations in distance to breakup in the case of horizontally displaced drops. First, small uncertainties in the initial configuration were unavoidable because the needle had to be moved between the successive injections. Secondly, the three-dimensional nature of the flow field (present from the outset) seemed to increase sensitivity of the evolution to small configurational variations.

4.6. *Statistical uniformity of the particulate distribution over time*

Section 4.5 seems clearly to validate both the dimensionless scaling presented in §§ 2.1 and 2.2, and the basic premise of using Stokeslets without any modifications for the near-field interactions. One last fundamental assumption from § 2.3 must be addressed: maintenance of statistical uniformity over time for a particulate 'discretization' of a drop, be it with Stokeslets or with glass beads. This would definitively justify using a swarm of Stokelets to model liquid drops as well as suspension drops, and would have far-reaching implications for numerical simulation of interfacial deformations that are impossible to track with a boundary method. The phenomena described here certainly fall into this category.

The considerable and accumulating weight of scientific literature that corroborates the correspondence between liquid drops and suspension drops should alone allay doubts on statistical uniformity. Moreover, the fact that the $1/r$ singularity of the Stokelet does not in any discernible way detract from the numerical results indicates that bunching so as to give serious velocity fluctuations does not occur (we have also spot checked the calculations with a flag for close approaches). All of this, of course, is no theoretical proof that statistical fluctuations for a fine discretization cannot manifest some systematic dynamic consequence, i.e. a substructural effect beyond continuum hydrodynamics, as embodied in the term blob (see § 1.6). Broad and comprehensive as the coverage of this paper already is, we leave the theoretical question to a future investigation. In the meantime, we can offer a statistical analysis of the computed particulate distributions to demonstrate the 'what' if not the 'why'.

To calculate the local number density as a function of position $\boldsymbol{x}$ in the swarm,

we need a procedure that corrects for the case where the averaging volume – here a sphere $\mathscr{B}(\boldsymbol{x};R)$ of radius R centred at $\boldsymbol{x}$ – extends partly outside the swarm; otherwise we will obtain a spuriously low value of the local density. Given only the coordinates of the Stokeslets, our method must automatically locate $\boldsymbol{x}$ in relation to the fuzzy interface, which we assume to be locally planar for small R. This amounts to a very specific kind of 'image processing'.

Consider an arbitrary density function $\rho(\boldsymbol{x})$ defined on one side of a planar interface. We denote by $\mathscr{B}_{\mathrm{i}}(\boldsymbol{x};R)$ the subset of $\mathscr{B}(\boldsymbol{x};R)$ that lies inside the domain, at a normal distance ζR in from the boundary. Using a Taylor expansion of ρ about $\boldsymbol{x}$, a weighted first moment of the density distribution within $\mathscr{B}_{\mathrm{i}}(\boldsymbol{x};R)$ can be related to ζ:

$$\boldsymbol{W}(\boldsymbol{x};R)\overset{\text{def}}{=}\left\{R\int_{\mathscr{B}_{\mathrm{i}}(\boldsymbol{x};R)}\rho(\boldsymbol{y})\,\mathrm{d}\mathscr{V}[\boldsymbol{y}]\right\}^{-1}\int_{\mathscr{B}_{\mathrm{i}}}\rho(\boldsymbol{y})(\boldsymbol{x}-\boldsymbol{y})\,\mathrm{d}\mathscr{V}[\boldsymbol{y}]=F(\zeta)\boldsymbol{n}+O(R),\quad(19)$$

with $\boldsymbol{n}$ the outward-pointing unit normal vector and

$$F(\zeta)=\begin{cases}1, & \zeta=-1\\ (\frac{3}{4})(1-\zeta^2)^2/(2+3\zeta-\zeta^3), & -1<\zeta<1\\ 0, & \zeta\geqslant 1.\end{cases}\quad(20)$$

Note that ζ is positive (negative) when $\boldsymbol{x}$ lies inside (outside) the domain. In terms of ζ the volume of $\mathscr{B}_{\mathrm{i}}$ is $V_{\mathrm{i}}(\boldsymbol{x};R)=4\pi R^3G(\zeta)/3$, with

$$G(\zeta)=\begin{cases}0, & \zeta\leqslant -1\\ \frac{1}{4}(2+3\zeta-\zeta^3), & -1<\zeta<1\\ 1, & \zeta\geqslant 1.\end{cases}\quad(21)$$

Thus we find for the average density

$$\bar{\rho}(\boldsymbol{x};R)\overset{\text{def}}{=}\frac{1}{V_{\mathrm{i}}(\boldsymbol{x};R)}\int_{\mathscr{B}_{\mathrm{i}}(\boldsymbol{x};R)}\rho(\boldsymbol{y})\,\mathrm{d}\mathscr{V}[\boldsymbol{y}]=\rho(\boldsymbol{x})-RF(\zeta)\boldsymbol{n}\cdot\nabla\rho(\boldsymbol{x})+O(R^2).\quad(22)$$

Applied to a discrete swarm instead of a continuous variation in density, we denote by $M_{\mathrm{i}}(\boldsymbol{x};R)$ the number of points $\boldsymbol{x}_m$ that lie inside $\mathscr{B}_{\mathrm{i}}(\boldsymbol{x};R)$, and compute the first moment with the summed version of equation (19):

$$\boldsymbol{W}(\boldsymbol{x};R)\approx\frac{1}{RM_{\mathrm{i}}(\boldsymbol{x};R)}\sum_{\boldsymbol{x}_m\in\mathscr{B}_{\mathrm{i}}(\boldsymbol{x};R)}(\boldsymbol{x}-\boldsymbol{x}_m)\quad(23)$$

Then ζ can be extracted from the implicit equation $\|\boldsymbol{W}\|=F(\zeta)$, and used to determine the local average number density,

$$\bar{\rho}(\boldsymbol{x};R)\approx\frac{3M_{\mathrm{i}}(\boldsymbol{x};R)}{4\pi R^3G(\zeta)}.\quad(24)$$

For a spherical swarm (parameter set E6 in table 2) we have used equations (21), (23) and (24) to track the average $\langle\bar{\rho}\rangle$ over all particles of the local number density $\bar{\rho}$, as well as the standard deviation σ about this mean. Particles left behind in a very thin tail (see Nitsche & Batchelor 1997) are not included in the average. Over a settling distance of 152 radii, both $\langle\bar{\rho}\rangle$ and σ remained nearly constant at their initial values: $1150<\langle\bar{\rho}\rangle<1194$, $6.8\%<\sigma<9.2\%$. Thus, after a very long history of mixing in the recirculating streamlines, there was no significant statistical redistribution of particles.

5. Conclusions

This paper has elucidated the coalescence, torus formation and breakup of sedimenting drops at zero Reynolds number and in the absence of both an interfacial tension and a viscosity difference between drops and ambient liquid. We have argued that liquid drops and suspension drops behave in fundamentally the same way inasmuch as the latter represent an accurate volumetric discretization of the excess mass present in the former. This volumetric discretization can be exploited for simple yet exceedingly robust numerical simulations based only upon a swarm of Stokeslets, since only the $1/r$ far-field interactions between particles is important. The numerical simulations track shape instabilities through the entire sequence of experimental phenomena: (i) deformation of the initial shape(s) into a (closed) torus, including axisymmetric and non-axisymmetric entrainment of liquid and coalescence, (ii) cyclic expansion and contraction of the torus, (iii) transition to an open torus and bulging, (iv) disintegration and the cascade of breakups. Our simulations show that the sequence (i–iv) is entirely explicable within the realm of Stokes flow, and neither interfacial tension nor inertia need be invoked in the mechanism. In the third stage we found a surprising sensitivity of the streamline pattern to the instantaneous shape of the ring. Even for such linear flows, the shape evolution is an inherently nonlinear instability.

So far the boundary-element method has been able to clarify the first effect mentioned above, but only up to the point where the interfaces pinch off or coalesce. In the past the evolution of the torus was considered either qualitatively (Joseph & Renardy 1993) or asymptotically based on the premise of a slender, axisymmetric open torus (Kojima *et al.* 1984). Our results indicate that this assumption is tenuous; a complete mechanistic explanation can be made without it.

Despite what might initially seem like a fairly poor discretization error in the Stokeslet simulations, a surprisingly small number of particles (less than 7000) reproduce the purely fluid mechanical behaviour, apparently without the obscuring influence of significant substructural effects. The generality of problems that can be addressed by our approach suggests applications to bubbles in fluidized beds (Batchelor 1974) as the conceptual inverse of the case studied here. We foresee extending the Stokeslet technique to include interfacial tension and different viscosities of the drop(s) and the ambient liquid – both of which are subjects of our active research. With regard to future experimental work, we would like to explore the dependence of hydrodynamic dispersion on the interparticle length scale, as well as the bulging instability of the tail.

This work benefited from a series of helpful conversations with Professor Johannes M. Nitsche, for which we are grateful. L.C.N. would like to thank his coauthors for fruitful collaboration, kind hospitality, and a most enlightening atmosphere during his sabbatical visit to the Institut für Strömungslehre und Wärmeübertragung at Technische Universität Graz. His financial support in the form of a Fulbright Senior Scholar Award, and from the Christian Doppler Laboratory for Continuous Solidification Processes, Vienna is gratefully acknowledged. Finally, thanks are due to three anonymous referees for their perceptive comments, questions and suggestions.

In memoriam (May 2000)

Uwe Schaflinger died peacefully on April 27, 2000 surrounded by his family. He was 51 years old. Uwe understood that science, family, conversation, the practical, the abstract, the trivial and the deep are all one and the same – life. Because of everything

we shared, working hard with Uwe came easy. We are grateful for the chance to walk part of the way with him.

REFERENCES

Adachi, K., Kiriyama, S. & Koshioka, N. 1978 The behaviour of a swarm of particles moving in a viscous fluid. *Chem. Engng Sci.* **33**, 115–121.

Arecchi, F. T., Buah-Bassuah, P. K., Francini, F., Pérez-Garcia, C. & Quercioli, F. 1989 An experimental investigation of the break-up of a liquid drop falling in a miscible fluid. *Europhys. Lett.* **9**, 333–338.

Batchelor, G. K. 1974 Low-Reynolds-number bubbles in fluidised beds. *Arch. Mech.* **26**, 339–351.

Boffetta, G., Cencini, M., Espa, S. & Querzoli, G. 2000 Chaotic advection and relative dispersion in an experimental convective flow. *Phys. Fluids* **12**, 3160–3167.

Brady, J. F. & Bossis, G. 1988 Stokesian dynamics. *Ann. Rev. Fluid Mech.* **20**, 111–157.

Brenner, H. 1980 Dispersion resulting from flow through spatially periodic porous media. *Phil. Trans. R. Soc. Lond.* A **297**, 81–133.

Brenner, M. P. 1999 Screening mechanisms in sedimentation. *Phys. Fluids* **11**, 754–772.

Clarke, A. T., Lal, M., Ruddock, J. N. & Warren, P. B. 2000 Mesoscopic simulation of drops in gravitational and shear fields. *Langmuir* **16**, 6342–6350.

Cristini, V., Blawzdziewicz, J. & Loewenberg, M. 1998 Drop breakup in three-dimensional viscous flows. *Phys. Fluids* **10**, 1781–1783.

Davis, R. H. 1996 Hydrodynamic diffusion of suspended particles: a symposium. *J. Fluid Mech.* **310**, 325–335.

Davis, R. H. 1999 Buoyancy-driven viscous interaction of a rising drop with a smaller trailing drop. *Phys. Fluids* **11**, 1016–1028.

Fountain, G. O., Khakhar, D. V., Mezic, I. & Ottino, J. M. 2000 Chaotic mixing in a bounded three-dimensional flow. *J. Fluid Mech.* **417**, 265–301.

Greenspan, D. 1990 Quasimolecular simulation of large liquid drops. *Int. J. Numer. Meth. Fluids* **10**, 247–257.

Jones, J. L., Lal, M., Ruddock, J. N. & Spenley, N. A. 1999 Dynamics of a drop at a liquid/solid interface in simple shear fields: a mesoscopic simulation study. *Faraday Discuss.* **112**, 129–142.

Joseph, D. D. & Renardy, Y. Y. 1993 *Fundamentals of Two-Fluid Dynamics.* Springer.

Koh, C. J. & Leal, L. G. 1989 The stability of drop shapes for translation at zero Reynolds number through quiescent fluid. *Phys. Fluids* A **1**, 1309–1313.

Koh, C. J. & Leal, L. G. 1990 An experimental investigation on the stability of viscous drops translating through a quiescent fluid. *Phys. Fluids* A **2**, 2103–2109.

Kojima, M., Hinch, E. J. & Acrivos, A. 1984 The formation and expansion of a toroidal drop moving in a viscous fluid. *Phys. Fluids* **27**, 19–32.

Kushner, J., IV, Rother, M. A. & Davis, R. H. 2001 Buoyancy-driven interactions of viscous drops with deforming interfaces. *J. Fluid Mech.* (in press).

Manga, M. 1996 Waves of bubbles in basaltic magmas and lavas. *J. Geophys. Res.* **101**, 17457–17465.

Manga, M. 1997 Interactions between mantle diapirs. *Geophys. Res. Lett.* **24**, 1871–1874.

Manga, M., Castro, J., Cashman, K. V. & Loewenberg, M. 1998 Rheology of bubble-bearing magmas. *J. Volcan. Geotherm. Res.* **87**, 15–28.

Manga, M. & Stone, H. A. 1993 Buoyancy-driven interactions between two deformable viscous drops. *J. Fluid Mech.* **256**, 647–683.

Manga, M. & Stone, H. A. 1994 Interactions between bubbles in magmas and lavas: effects of bubble deformation. *J. Volcan. Geotherm. Res.* **63**, 267–279.

Manga, M. & Stone, H. A. 1995 Collective hydrodynamics of deformable drops and bubbles in dilute low Reynolds number suspensions. *J. Fluid Mech.* **300**, 231–263.

Manga, M., Stone, H. A. & O'Connell, R. J. 1993 The interaction of plume heads with compositional discontinuities in the Earth's mantle. *J. Geophys. Res.* **98**, 19979–19990.

Moseler, M. & Landman, U. 2000 Formation, stability and breakup of nanojets. *Science* **289**, 1165–1169.

Murad, S. & Law, C. K. 1999 Molecular simulation of droplet collision in the presence of ambient gas. *Molec. Phys.* **96**, 81–85.

Nitsche, J. M. & Batchelor, G. K. 1997 Break-up of a falling drop containing dispersed particles. *J. Fluid Mech.* **340**, 161–175.

Nitsche, L. C. & Brenner, H. 1989 Eulerian kinematics of flow through spatially periodic models of porous media. *Arch. Rat. Mech. Anal.* **107**, 225–292.

Ottino, J. M. 1989 *The Kinematics of Mixing: Stretching, Chaos, and Transport*. Cambridge University Press.

Ottino, J. M. 1990 Mixing, chaotic advection, and turbulence. *Ann. Rev. Fluid Mech.* **22**, 207–253.

Pozrikidis, C. 1990 The instability of a moving viscous drop. *J. Fluid Mech.* **210**, 1–21.

Pozrikidis, C. 1992 *Boundary Integral and Singularity Methods for Linearized Viscous Flow*. Cambridge University Press.

Press, W. H., Flannery, B. P., Teukolsky, S. A. & Vetterling, W. T. 1992 *Numerical Recipes in C: The Art of Scientific Computing*, 2nd Edn. Cambridge University Press.

Rallison, J. M. 1981 A numerical study of the deformation and burst of a viscous drop in general shear flows. *J. Fluid Mech.* **109**, 465–482.

Rother, M. A., Zinchenko, A. Z. & Davis, R. H. 1997 Buoyancy-driven coalescence of slightly deformable drops. *J. Fluid Mech.* **346**, 117–148.

Schaflinger, U. & Machu, G. 1999 Interfacial phenomena in suspensions. *Chem. Engng Technol.* **22**, 617–619.

Stone, H. A. 1994 Dynamics of drop deformation and breakup in viscous fluids. *Ann. Rev. Fluid Mech.* **26**, 65–102.

Thomson, J. J. & Newall, H. F. 1885 On the formation of vortex rings by drops falling into liquids, and some allied phenomena. *Proc. R. Soc. Lond.* **39**, 417–435.